

# Accelerating proximal Markov chain Monte Carlo by using explicit stabilised methods

Luis Vargas<sup>1,2,3</sup>Marcelo Pereyra<sup>2,3</sup>Konstantinos C. Zygalakis<sup>1,3</sup>

December 21, 2024

## Abstract

We present a highly efficient proximal Markov chain Monte Carlo methodology to perform Bayesian computation in imaging problems. Similarly to previous proximal Monte Carlo approaches, the proposed method is derived from an approximation of the Langevin diffusion. However, instead of the conventional Euler-Maruyama approximation that underpins existing proximal Monte Carlo methods, here we use a state-of-the-art orthogonal Runge-Kutta-Chebyshev stochastic approximation [2] that combines several gradient evaluations to significantly accelerate its convergence speed, similarly to accelerated gradient optimisation methods. For Gaussian models, we prove rigorously the acceleration of the Markov chains in the 2-Wasserstein distance as a function of the condition number  $\kappa$ . The performance of the proposed method is further demonstrated with a range of numerical experiments, including non-blind image deconvolution, hyperspectral unmixing, and tomographic reconstruction, with total-variation and  $\ell_1$ -type priors. Comparisons with Euler-type proximal Monte Carlo methods confirm that the Markov chains generated with our method exhibit significantly faster convergence speeds, achieve larger effective sample sizes, and produce lower mean square estimation errors at equal computational budget.

## 1 Introduction

Imaging sciences study theory, methods, models, and algorithms to solve imaging problems, such as image denoising [30], deblurring [9, 5], compressive sensing reconstruction [35], super-resolution [48], tomographic reconstruction [5], inpainting [56], source separation [31], and phase retrieval [22].

There are currently three main formal paradigms to formulate and solve imaging problems: the variational framework [16], machine learning [6], and the Bayesian statistical framework [46, 44]. In this paper we focus on the Bayesian framework, which is an intrinsically probabilistic paradigm where the data observation process and the prior knowledge available are represented by using statistical models, and where solutions are derived by using inference techniques stemming from Bayesian decision theory [46, 41]. The Bayesian framework is particularly well equipped to address imaging problems in which uncertainty plays an important role, such as medical imaging or remote sensing problems where it is necessary or desirable to quantify the uncertainty in the delivered solutions to inform decisions or conclusions (see, e.g., [40, 45, 12]). The framework is also well adapted to blind, semi-blind, and unsupervised problems involving partially unknown models (e.g., unspecified regularisation parameters or observation operators) [55, 42, 24]. Bayesian model selection technique also allow the objective comparison of several potential models to analyse the observed imaging data, even in cases where there is no ground truth available [20, 43].

In this paper we focus on the computational aspects of performing Bayesian inferences in imaging problems. Modern Bayesian computation methods suitable for imaging sciences can be broadly grouped in three categories (please see [44] for a recent survey on the topic): stochastic Markov chain Monte Carlo (MCMC) methods that are computationally expensive but robust, and which can be applied to a wide range of models and inferences; optimisation methods that are significantly more efficient by comparison, but which are only useful for point estimation and some other

---

<sup>1</sup>School of Mathematics, University of Edinburgh, Edinburgh, Scotland

<sup>2</sup>School of Mathematical and Computer Sciences, Heriot-Watt University, Edinburgh, Scotland

<sup>3</sup>Maxwell Institute for Mathematical Sciences, Bayes Centre, 47 Potterrow, Edinburgh, Scotland

specific inferences; and deterministic approximation methods such as variational Bayes and message passing methods, which are efficient and support more complex inferences, but can only be applied to specific models, have little theory, and often exhibit convergence issues. Recently, there have been significant advances in MCMC methodology for imaging, particularly for Bayesian models that are log-concave w.r.t. the unknown image, for which maximum-a-posteriori estimation is a convex optimisation problem. This paper seeks to further improve MCMC methodology for imaging.

MCMC methods were already actively studied in the imaging literature two decades ago, and have regained attention lately because of their capacity to address challenging imaging problems that are beyond the scope of optimisation-based and machine learning techniques. In particular, the interface between MCMC and optimisation has become a very active research area, especially around the so-called proximal MCMC algorithms [39, 20] that combine ideas from high-dimensional stochastic simulation with techniques from convex analysis and proximal optimisation to achieve better computational efficiency. Despite being relatively recent, proximal MCMC methods have already been successfully applied to a range of Bayesian inference problems, for example, image deconvolution with total-variation and wavelet priors [20, 53], inpainting [53], tomographic reconstruction [20], astronomical imaging [12], restoration of images corrupted by Poisson noise [52], ultrasound imaging [36], image coding [23], sparse binary logistic regression [51], and graph processing [10].

This paper seeks to exploit recent developments in stochastic numerical analysis to significantly improve the computational efficiency of proximal MCMC methodology. More precisely, we propose to use a state-of-the-art orthogonal Runge-Kutta-Chebyshev stochastic approximation of the Langevin diffusion process [2] that is significantly more computationally efficient than the conventional Euler-Maruyama approximation used by existing proximal MCMC methods. In particular, we present a new proximal MCMC method that applies this approximation to the Moreau-Yoshida regularised Langevin diffusion underpinning the Moreau-Yoshida unadjusted Langevin algorithm [20], and show both theoretically and empirically that this leads to dramatic improvements in convergence speed and estimation accuracy.

The remainder of the paper is organised as follows: Section 2 defines notation, introduces the class of models considered, and recalls the Moreau-Yoshida unadjusted Langevin algorithm that is the basis of our method. In Section 3 we present the proposed MCMC method and analyse its theoretical convergence and stability properties. Section 4 illustrates the methodology in two one-dimensional toy problems, as well as with three experiments related to image deconvolution, hyper-spectral unmixing, and tomographic reconstruction, where we report detailed comparisons with the Moreau-Yoshida unadjusted Langevin algorithm [20]. Conclusions and perspectives for future work are reported in Section 5. Proofs are finally reported in Appendices A and B.

## 2 Problem statement

### 2.1 Bayesian inference for imaging inverse problems

We consider imaging problems involving an unknown image  $x \in \mathbb{R}^d$  and some observed data  $y \in \mathbb{C}^p$ , related to  $x$  through a statistical model with likelihood function  $p(y|x)$ . In particular, we are interested in problems where the recovery of  $x$  from  $y$  is ill-conditioned or ill-posed. For example, problems of the form  $y = Ax + w$  with  $w \sim \mathcal{N}(0, \sigma^2 \mathbb{I}_p)$  and  $\sigma > 0$  where the observation operator  $A \in \mathbb{C}^{n \times p}$  is rank deficient or has a poor condition number. As mentioned previously, such problems are ubiquitous in imaging sciences and have been the focus of significant research efforts [50, 17].

In this paper we adopt a Bayesian approach to regularise the estimation problem and deliver meaningful estimates of  $x$ , as well as uncertainty quantification for the solutions delivered. More precisely, we represent  $x$  as a random quantity with prior distribution  $p(x)$  promoting expected properties (e.g., sparsity, piecewise-regularity, smoothness, etc.), and base our inferences on the posterior distribution [32]

$$\pi(x) \triangleq p(x|y) = \frac{p(y|x)p(x)}{\int_{\mathbb{R}^d} p(y|x)p(x)dx}, \quad (2.1)$$

which we henceforth denote by  $\pi$ . We focus on models of the following form

$$\pi(x) = \frac{e^{-U(x)}}{\int_{\mathbb{R}^d} e^{-U(s)} ds}, \quad (2.2)$$

where the potential  $U$  admits a decomposition  $U = f + g$ , where  $f : \mathbb{R}^d \rightarrow \mathbb{R}$  and  $g : \mathbb{R}^d \rightarrow (-\infty, \infty]$  are two lower bounded functions satisfying the following conditions:

1.  $f$  is convex and Lipschitz continuously differentiable with constant  $L_f$ , i.e.,

$$\|\nabla f(x) - \nabla f(y)\|_2 \leq L_f \|x - y\|_2, \quad \forall x, y \in \mathbb{R}^d,$$

2.  $g$  is proper, convex, and lower semi continuous, but potentially non-smooth.

This class of models is widely used in imaging sciences, and includes, for instance, analysis models of the form  $f(x) = \|y - Ax\|^2/2\sigma^2$  and  $g(x) = \theta\|\Psi x\|_{\dagger} + \iota_{\mathcal{S}}(x)$  some dictionary or representation  $\Psi$  and norm or pseudo-norm  $\|\cdot\|_{\dagger}$ , and a hard constraint  $\mathcal{S} \subset \mathbb{R}^d$  on the solution space<sup>1</sup>.

Posterior distributions of the form (2.2) are log-concave, which is an important property for Bayesian inference because it guarantees the existence of all posterior moments and hence of moment-based estimators such as the minimum mean squared error (MMSE) estimator [41]. Log-concavity also plays a central role in maximum-a-posteriori (MAP) estimation [41], given by

$$\begin{aligned} \hat{x}_{MAP} &= \arg \max_x \pi(x) \\ &= \arg \min_x f(x) + g(x) \end{aligned}$$

which is the predominant estimation strategy in imaging sciences. The popularity of MAP estimation stems from the fact that it is a convex optimisation problem that can be efficiently solved by using modern proximal splitting optimisation techniques [16]. This is a strong computational advantage w.r.t. other estimation strategies that require calculating probabilities and expectations of  $x|y$  [27, 44]. There are also theoretical reasons why MAP estimation performs well in high-dimensional models that are log-concave (see [41] for details). Moreover, some forms of approximate uncertainty quantification can be also be formulated as convex optimisation problems and efficiently solved by using proximal splitting techniques. [40, 12, 45].

However, most Bayesian analyses require using specialised computational statistics techniques to calculate expectations and probabilities w.r.t.  $\pi$ . For example, computing Bayesian estimators (e.g., MMSE estimation), calibrating unknown model parameters (e.g., regularisation parameters), performing Bayesian model selection and predictive model checks, and reporting (exact) credible regions and hypothesis tests. From a Bayesian computation viewpoint, this typically requires using a high-dimensional Markov chain Monte Carlo (MCMC) method to simulate samples from  $x|y$  followed by Monte Carlo integration [27, 44]. Unfortunately, this approach has been traditionally too computationally expensive for wide adoption in imaging sciences, limiting the impact of Bayesian statistics in this field. Alternatively, one can also perform approximate inferences by using deterministic surrogate methods, such as variational Bayes approximations (see the recent survey [44]). However, deterministic approximations are problem-specific, can exhibit convergence issues, and have little theoretical guarantees, and hence they have not been widely adopted either.

Recent works have sought to address these limitation of Bayesian computation methodology by developing new and highly efficient MCMC methods tailored for imaging sciences, particularly by using techniques from proximal optimisation that are already widely adopted in the field. These so-called proximal MCMC methods [39, 20, 53, 10] have been an important step towards promoting Bayesian imaging techniques, as they are easy to implement, have significantly reduced computing times, and improve theoretical guarantees on the solutions delivered. However, there remain some fundamental features of modern optimisation methodology that have not yet been replicated in proximal MCMC approaches. In particular, modern optimisation methods rely strongly on acceleration techniques to achieve faster convergence rates and improve their robustness to poor conditioning [54]. In this paper, we accelerate proximal MCMC methods to improve their convergence properties.

---

<sup>1</sup>For any  $\mathcal{S} \subset \mathbb{R}^d$ , the indicator  $\iota_{\mathcal{S}}$  takes value  $\iota_{\mathcal{S}}(x) = 0$  if  $x \in \mathcal{S}$ , and  $\iota_{\mathcal{S}}(x) = +\infty$  otherwise.

## 2.2 Bayesian computation for imaging inverse problems

### 2.2.1 Langevin Markov chain Monte Carlo methods

Proximal MCMC methods are derived from the overdamped Langevin diffusion, which we recall below. For clarity we first introduce the approach for models that are smooth, and then explain the generalisation to non-smooth models.

Suppose the need to sample from a high-dimensional density  $\bar{\pi}$  that is continuously differentiable on  $\mathbb{R}^d$ . Langevin MCMC methods address this task by using the overdamped Langevin stochastic differential equation (SDE), given by

$$dX_t = \nabla \log \bar{\pi}(X_t) dt + \sqrt{2} dW_t \quad (2.3)$$

where  $(W_t)_{t \geq 0}$  is a  $d$ -dimensional Brownian motion. Under mild regularity assumptions, this SDE has a unique strong solution and admits  $\bar{\pi}$  as unique invariant distribution. Consequently, if we could solve (2.3) and let  $t \rightarrow \infty$ , this would provide Monte Carlo samples from  $\bar{\pi}$  useful for Bayesian computation. This strategy is particularly computationally efficient when  $\bar{\pi}$  is log-concave because in that case  $X_t$  converges in distribution to  $\bar{\pi}$  exponentially fast with a good rate [19].

Unfortunately, it is generally not possible to exactly solve (2.3), and discrete approximations of  $X_t$  need to be considered instead. In particular, most algorithms use the Euler-Maruyama (EM) discretization [34]:

$$X_{n+1} = X_n + \delta \nabla \log \bar{\pi}(X_n) + \sqrt{2\delta} Z_{n+1}, \quad (2.4)$$

where  $\delta > 0$  is a given stepsize and  $(Z_n)_{n \geq 1}$  is a sequence of i.i.d.  $d$ -dimensional standard Gaussian random variables. This MCMC method is known as the unadjusted Langevin algorithm (ULA) [47].

Under some regularity assumptions, namely  $\bar{L}$ -Lipschitz continuity of  $\nabla \log \bar{\pi}$  and  $\delta < 2/\bar{L}$ , the Markov chain  $(X_n)_{n \geq 0}$  is ergodic with stationary distribution  $\bar{\pi}_\delta(x)$  close to  $\bar{\pi}$  [19]. Additionally, when  $\bar{\pi}$  is log-concave, ULA inherits the favourable properties of (2.3) and converges to  $\bar{\pi}_\delta(x)$  geometrically fast with good convergence rates, offering an efficient Bayesian computation methodology for large problems [19].

The estimation bias [4] associated with targeting  $\bar{\pi}_\delta(x)$  instead of  $\bar{\pi}$  can be reduced by decreasing  $\delta$ , and vanishes as  $\delta \rightarrow 0$ . However, decreasing  $\delta$  deteriorates the convergence properties of the chain and amplifies the associated non-asymptotic bias and variance. Therefore, to apply ULA to large problems in a computationally efficient way it is necessary to use values of  $\delta$  that are close to the stability limit  $2/\bar{L}$ , at the expense of some asymptotic bias. Notice that it is also possible to remove the asymptotic bias by combining ULA with a Metropolis-Hastings correction step targeting  $\bar{\pi}$ , leading to the so-called Metropolis adjusted Langevin algorithm (MALA) [47]. This strategy is widely used in computational statistics for medium-sized problems. However, in large problems such as imaging problems, using a Metropolis-Hastings correction may dramatically deteriorate the convergence speed [20].

### 2.2.2 Proximal Markov chain Monte Carlo methods

We now consider the class of models  $\pi$  given by (2.2), which are not smooth. Unfortunately, ULA and MALA cannot be directly applied to such models, as they require Lipschitz differentiability of  $\log \pi$ . Proximal MCMC methods address this difficulty by carefully constructing a smooth approximation  $\pi^\lambda$  that by construction satisfies all the regularity conditions required by ULA and MALA, and which can be made arbitrarily close to the original model  $\pi$  by tuning a regularisation parameter  $\lambda > 0$ . This strategy, originally proposed in [39], can be implemented in different ways. In particular, [20] replaces the non-smooth term  $g$  in (2.2) with its Moreau-Yosida (MY) envelope

$$g^\lambda(x) = \min_{y \in \mathbb{R}^d} \left\{ g(y) + \frac{1}{2\lambda} \|x - y\|^2 \right\}.$$

to construct the approximation

$$\pi^\lambda(x) = \frac{e^{-f(x) - g^\lambda(x)}}{\int_{\mathbb{R}^d} e^{-f(s) - g^\lambda(s)} ds},$$

which has the following key properties that are useful for Bayesian computation [20]:

- For all  $\lambda > 0$ ,  $\pi^\lambda$  defines a proper density on  $\mathbb{R}^d$ .

- For all  $\lambda > 0$ ,  $\pi^\lambda$  is log-concave and Lipschitz continuously differentiable with

$$\begin{aligned}\nabla \log \pi^\lambda &= -\nabla f(x) - \nabla g^\lambda(x), \\ &= -\nabla f(x) - \frac{1}{\lambda} (x - \text{prox}_g^\lambda(x)),\end{aligned}\tag{2.5}$$

with Lipschitz constant  $L = L_f + 1/\lambda$ , and where for all  $x \in \mathbb{R}^d$

$$\text{prox}_g^\lambda(x) = \arg \min_{u \in \mathbb{R}^d} g(u) + \frac{1}{2\lambda} \|x - u\|^2.$$

- The approximation  $\pi^\lambda$  converges to  $\pi$  in total-variation norm; i.e.,

$$\lim_{\lambda \rightarrow 0} \|\pi^\lambda - \pi\|_{TV} = 0.$$

Given the smooth approximation  $\pi^\lambda$ , we define the auxiliary Langevin SDE

$$dX_t = \nabla \log \pi^\lambda(X_t) dt + \sqrt{2} dW_t\tag{2.6}$$

and derive the MYULA Markov chain by discretising this SDE by the EM method

$$X_{n+1} = X_n - \delta \nabla f(X_n) - \frac{\delta}{\lambda} (X_n - \text{prox}_g^\lambda(X_n)) + \sqrt{2\delta} Z_{n+1}.\tag{2.7}$$

If necessary, the asymptotic bias can then be removed by complementing MYULA with a Metropolis-Hastings step [39], which is useful for benchmarking purposes [20, 12]. Notice that one can also consider other approximations constructed by applying the Moreau-Yosida envelope directly to  $f + g$  [39], or by replacing the Moreau-Yosida envelope with a forward-backward envelope [39, 7]. It is also possible to apply the Moreau-Yosida envelope separately to  $f$  and  $g$  and integrate MYULA (with or without Metropolisation) within an auxiliary-variable Gibbs sampling scheme (see [53]).

As mentioned previously, despite being relatively recent, proximal MCMC methods have already been successfully applied to a range of large-scale Bayesian inference problems related to imaging sciences [20, 12, 53, 36], and machine learning [23, 51, 10, 11].

### 2.2.3 Limitations of proximal Markov chain Monte Carlo methods

A main limitation of ULA, MALA and their proximal variants is that they are all derived from the EM approximation (2.4) of the Langevin SDE. This approximation is mainly used because it is computationally efficient in high-dimensions, it is easy to implement, and it can be rigorously theoretically analysed. However, the EM approximation is not particularly suitable for problems that are ill-conditioned or ill-posed as its performance is very sensitive to the anisotropy of the target density, which is a common feature of imaging problems. More precisely, in order to be useful for Bayesian computation, the EM approximation of the Langevin SDE (2.6) has to be numerically stable. For MYULA, this requires using a stepsize  $\delta < 2/L$  with  $L = L_f + 1/\lambda$ , where we recall that  $L_f$  is the Lipschitz constant of  $\nabla f$  and that  $\lambda$  controls the quality of the approximation  $\pi_\lambda$  of  $\pi$ . This restriction essentially guarantees that the chain moves slowly enough to follow changes in  $\nabla \log \pi_\lambda$  in a numerically stable manner, particularly along directions of fast change. However, this is problematic when  $\pi_\lambda$  has some directions or regions of the parameter space that change relatively very slowly, as the chain will struggle to properly explore the solution space and will require a very large number of iterations to converge. In imaging models, this typically arises when the likelihood  $p(y|x)$  has identifiability issues (e.g. if it involves an observation operator  $A$  for which  $A^\top A$  is badly conditioned or rank deficient), or if we seek to use a small value of  $\lambda$  to bring  $\pi_\lambda$  close to  $\pi$ .

To highlight this issue, we report below two simple illustrative experiments where MYULA is applied to a two-dimensional Gaussian distribution. In this case there is no non-smooth term  $g$  and the time-step restriction is dictated by the Lipschitz constant of  $f$ , but the same phenomenon arises in more general models. In the first experiment

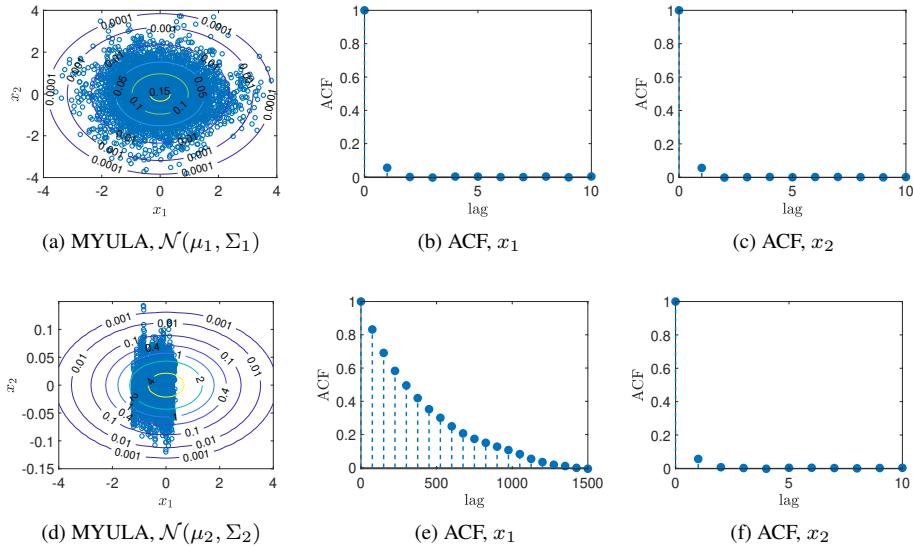


Figure 1: Two-dimensional Gaussian distribution: (a)  $5 \times 10^3$  samples generated by the MYULA algorithm using the target distributions  $\mathcal{N}(\mu_1, \Sigma_1)$  with  $\delta = 0.25$  and (d)  $\mathcal{N}(\mu_2, \Sigma_2)$  with  $\delta = 2.5 \times 10^{-4}$ . Autocorrelation functions of the (b)-(e) first and (c)-(f) second component (i.e.,  $x_1$  and  $x_2$ ) of the samples generated by the ULA algorithm, having  $\mathcal{N}(\mu_1, \Sigma_1)$  and  $\mathcal{N}(\mu_2, \Sigma_2)$  as target distributions, respectively.

we consider  $\mu_1 = (0, 0)$  and  $\Sigma_1 = \text{diag}(1, 1)$  (i.e.,  $L_f = 1$ ); whereas in the second experiment we use  $\mu_2 = (0, 0)$  and  $\Sigma_2 = \text{diag}(1, 10^{-3})$  (i.e.,  $L_f = 10^3$ ). The results are presented in Figure 1. Notice that in the first case MYULA explores the distribution very well, showing a good rate of decay in the autocorrelation functions of both components. However, in the second case, MYULA exhibits poor convergence properties as it struggles to explore the first component.

This limitation of the EM approximation could be partially mitigated by preconditioning the gradient  $\nabla \log \pi_\lambda$  as recommended in [26]. However, preconditioning in high dimensions is usually very computationally expensive (the development of efficient preconditioning strategies for imaging models is an active research topic, see, e.g., [38, 37]). Alternatively, one can also mitigate the limitations of the EM approximation by substituting both  $f$  and  $g$  with their regularised envelopes  $f^\lambda$  and  $g^\lambda$ , and using two MYULA steps with  $\delta = \lambda$ , but this introduces some additional approximation errors [53].

It is worth mentioning at this point that one can also consider other dynamics to derive Markov chains with potentially better convergence properties, namely the Hamiltonian dynamic which leads to the Hamiltonian Monte Carlo (HMC) algorithm [44, 14]. However, HMC uses a Verlet integrator that, despite being superior in other ways, has the same stepsize restrictions as the Euler method and hence also struggles to address problems that are poorly conditioned. Also, HMC uses a Metropolis correction that be dramatically inefficient in large problems such as imaging problems.

In this paper we propose to fundamentally improve proximal MCMC methods for imaging by using state-of-the-art numerical SDE approximation strategies that significantly outperform the conventional EM scheme. More precisely, we focus on a class of explicit stabilised methods that are specifically designed to deal with the time-step restriction, called stochastic orthogonal Runge-Kutta-Chebyshev methods (SK-ROCK) [2]. The idea, in a nutshell, is to cleverly combine several evaluations of the gradient  $\nabla \log \pi^\lambda(x)$  in a way that allows for taking larger time-steps, and thus breaking the stability barrier of MYULA. The same strategy can then be straightforwardly applied to other proximal MCMC methods that internally use MYULA (e.g., [53]), or variants of MYULA with other approximations of  $\pi$  (e.g., [39, 7]), although this is beyond the scope of this paper and will be investigated in future works.

The remainder of this paper is organized as follows: in Section 3 we introduce the proposed SK-ROCK proximal MCMC method, present an analysis of the Wasserstein distance between a general discretisation scheme and a

Gaussian target density, and show numerically the improvement one can get with the implementation of the stochastic ROCK method in terms of rates of convergence for large condition number of the covariance matrix. To demonstrate further the efficacy of these schemes, in Section 4 we present a number of numerical experiments on inference for simple one dimensional test problems as well three imaging inverse problems containing  $\ell_1$  and  $TV$  priors. Finally, we conclude in Section 5 where we also discuss future research directions.

### 3 Proposed Bayesian computation method

#### 3.1 Stochastic orthogonal Runge-Kutta-Chebyshev methods

We propose to significantly accelerate Bayesian computation for imaging problems by using the state-of-the-art explicitly stabilised SK-ROCK scheme [2] to approximate the Langevin SDE (2.6) associated with  $\pi_\lambda$ , instead of the basic EM discretisation scheme that underpins MYULA and other proximal MCMC methods. From a numerical analysis viewpoint, this is a highly advanced Runge-Kutta stochastic integration scheme that extends the deterministic Chebyshev method [1] to SDEs, and uses a damping strategy to stabilise the stochastic term. Crucially, its implementation is straightforward as it only requires knowledge of the gradient operator  $\nabla \log \pi^\lambda(x)$  given by (2.5), which is also used in MYULA. However, unlike MYULA that uses a single evaluation of  $\nabla \log \pi^\lambda(x)$  per iteration, the considered Runge-Kutta scheme performs  $s \in \mathbb{N}^*$  evaluations of  $\nabla \log \pi^\lambda(x)$  at carefully chosen extrapolated points determined by Chebyshev polynomials. In this regard, the stochastic integration scheme is morally similar to accelerated optimisation methods that also use several gradient evaluations and extrapolation techniques to significantly improve their convergence properties. In fact, the deterministic Runge-Kutta-Chebyshev method was recently shown to have similar theoretical convergence properties to Nesterov’s accelerated optimisation algorithms in the case of strongly convex functions [21].

The proposed proximal SK-ROCK method is presented in Algorithm 1 below, where  $T_s$  denotes the Chebyshev polynomial of order  $s$  of the first kind, defined recursively by  $T_{k+1} = 2xT_k(x) - T_{k-1}(x)$  with  $T_0(x) = 1$  and  $T_1(x) = x$ . Based on our experience, we recommend using this method with  $s \in \{3, \dots, 15\}$  to achieve a good bias-variance trade-off<sup>2</sup>; and note that setting  $s = 1$  reduces the methods to MYULA. Lastly, it is worth mentioning at this point that we also considered other alternatives to the EM scheme, namely the Runge-Kutta scheme of [3], but found that SK-ROCK delivers the best performance for imaging models (the results with alternative schemes are not reported in the paper because of lack of space).

#### 3.2 Illustrative example with a Gaussian target density

To illustrate the benefits of using the proximal SK-ROCK instead of MYULA method we repeat the Gaussian experiments reported in Figure 1 with Algorithm 1. The results are shown in Figure 2. Observe that because the SK-ROCK method is allowed to use a larger stepsize  $\delta$  in a stable manner, it produces, for the same computational cost, samples that are significantly less correlated than MYULA with respect to the slow component. We also observe in Figure 2 that this allows SK-ROCK to explore the target distribution more accurately.

These empirical observations can be formally derived by theoretically analysing the convergence properties of MYULA and SK-ROCK for a  $d$ -dimensional Gaussian target distribution with density  $\pi(x) \propto \exp(-0.5x^\top \Sigma^{-1}x)$ , and  $\Sigma = \text{diag}(\sigma_1^2, \dots, \sigma_d^2)$ . More precisely, we study how the methods converge in the 2-Wasserstein distance, as a function of the stepsize  $\delta$  and the number of iterations  $n$ . This is achieved by analysing in full generality the numerical solution of the Langevin SDE associated with  $\pi$ , given by

$$dX_t = -\Sigma^{-1}X_t dt + \sqrt{2}dW_t, \tag{3.1}$$

by a one step numerical integrator, which yields (in general) a recurrence of the form

$$X_{n+1}^i = R_1(z_i)X_n^i + \sqrt{2\delta}R_2(z_i)\xi_{n+1}^i, \quad \xi_{n+1}^i \sim N(0, 1), \tag{3.2}$$

---

<sup>2</sup>In principle one could take  $s$  to be arbitrary large, but this would lead to more biased solutions.

---

**Algorithm 1** SK-ROCK algorithm
 

---

**Set**  $X_0 \in \mathbb{R}^d$ ,  $\lambda > 0$ ,  $n \in \mathbb{N}$ ,  $s \in \{3, \dots, 15\}$ ,  $\eta = 0.05$

**Compute**  $l = (s - 0.5)^2(2 - 4/3\eta) - 1.5$

**Compute**

$$\omega_0 = 1 + \frac{\eta}{s^2}, \quad \omega_1 = \frac{T_s(\omega_0)}{T'_s(\omega_0)}, \quad \mu_1 = \frac{\omega_1}{\omega_0}, \quad \nu_1 = s\omega_1/2, \quad k_1 = s\omega_1/\omega_0$$

**Choose**  $\delta \in (0, l/(L_f + 1/\lambda)]$

**for**  $i = 0 : n$  **do**

$Z_{i+1} \sim \mathcal{N}(0, \mathbb{I}_d)$

$K_0 = X_i$

$K_1 = X_i + \mu_1 \delta \nabla \log \pi^\lambda(X_i + \nu_1 \sqrt{2\delta} Z_{i+1}) + k_1 \sqrt{2\delta} Z_{i+1}$

**for**  $j = 2 : s$  **do**

**Compute**

$$\mu_j = \frac{2\omega_1 T_{j-1}(\omega_0)}{T_j(\omega_0)}, \quad \nu_j = \frac{2\omega_0 T_{j-1}(\omega_0)}{T_j(\omega_0)}, \quad k_j = -\frac{T_{j-2}(\omega_0)}{T_j(\omega_0)} = 1 - \nu_j$$

$K_j = \mu_j \delta \nabla \log \pi^\lambda(K_{j-1}) + \nu_j K_{j-1} + k_j K_{j-2}$

**end for**

$X_{i+1} = K_s$

**end for**

---

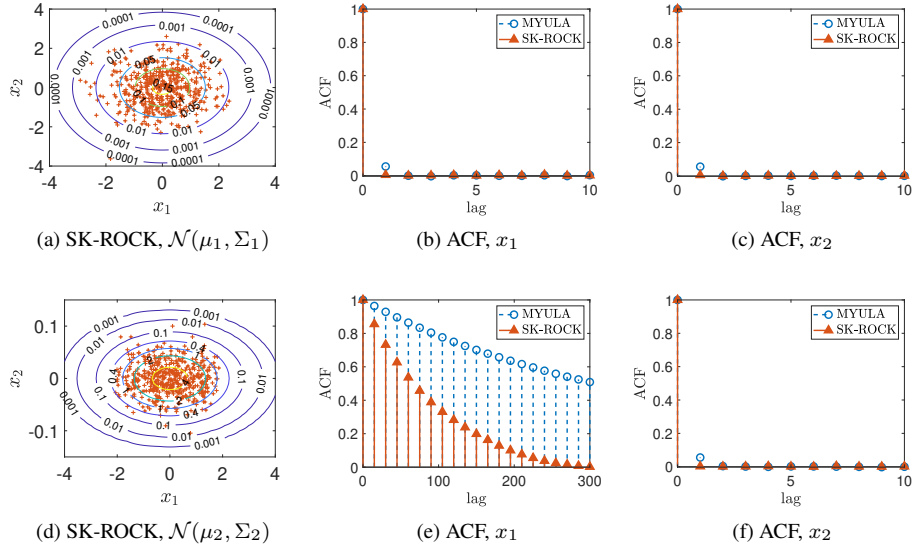


Figure 2: Two-dimensional Gaussian distribution: (a)  $5 \times 10^3/s$  samples generated by the SK-ROCK algorithm ( $s = 10$ ) using the target distribution  $\mathcal{N}(\mu_1, \Sigma_1)$  with  $\delta = 10.61$  and (d)  $\mathcal{N}(\mu_2, \Sigma_2)$  with  $\delta = 1.06 \times 10^{-2}$ . Autocorrelation functions of the (b)-(e) first and (c)-(f) second component (i.e.,  $x_1$  and  $x_2$ ) of the samples generated by the SK-ROCK algorithm, having  $\mathcal{N}(\mu_1, \Sigma_1)$  and  $\mathcal{N}(\mu_2, \Sigma_2)$  as target distributions, respectively.

where  $z_i = -\delta/\sigma_i^2$  and  $X_0 = (x_0^1, \dots, x_0^d)^T$  is a deterministic initial condition. For the EM scheme used in MYULA we have  $R_1(z) = 1 + z$  and  $R_2(z) = 1$ , and for the SK-ROCK we have that [2]

$$R_1(z) = \frac{T_s(\omega_0 + \omega_1 z)}{T_s(\omega_0)}, \quad R_2(z) = \frac{U_{s-1}(\omega_0 + \omega_1 z)}{U_{s-1}(\omega_0)} \left(1 + \frac{\omega_1}{2} z\right), \quad (3.3)$$

where  $T_s, U_s$  are Chebyshev polynomials of first and second kind respectively and

$$\omega_0 = 1 + \frac{\eta}{s^2}, \quad \omega_1 = \frac{T_s(\omega_0)}{T_s'(\omega_0)}.$$

By using the fact that Gaussian distributions are closed under linear transformations, and assuming that the initial condition  $X_0$  is deterministic, we derive the distribution of  $X_n$  for any  $\delta > 0$  and obtain the following result<sup>3</sup> :

**Proposition 3.1.** *Let  $\pi(x) \propto \exp(-0.5x^T \Sigma^{-1}x)$  with  $\Sigma = \text{diag}(\sigma_1^2, \dots, \sigma_d^2)$ , and let  $Q_n$  be the probability measure associated with  $n$  iterations of the generic Markov kernel (3.2). Then the 2-Wasserstein distance between  $\pi$  and  $Q_n$  is given by*

$$W_2(\pi; Q_n)^2 = \sum_{i=1}^d (D_n(z_i, x_0^i) + B_n(z_i, \sigma_i)), \quad (3.4)$$

where

$$D_n(x, u) = (R_1(x))^{2n} u^2, \quad B_n(x, u) = \left[ u - \sqrt{2\delta} R_2(x) \left( \frac{1 - (R_1(x))^{2n}}{1 - (R_1(x))^2} \right)^{1/2} \right]^2.$$

Observe that the  $W_2^2$  distance between  $\pi$  and  $Q_n$  involves two terms. The first term  $D_n$  vanishes as  $n \rightarrow \infty$ , and is closely related to the convergence rate of the chain. The second term  $B_n$  does not vanish as  $n$  increases, and is related to the asymptotic bias of the method [4] (recall that without a Metropolis correction step, any generic approximation of (3.1) will have some asymptotic bias because it will not exactly converge to  $\pi$ ). In order to gain insight for the complexity of the methods, one can use Proposition 3.1 to calculate how many steps  $n$  one needs to take in order for the error in (3.4) to be smaller than some  $\varepsilon^2$  factor. For the case of the EM (ULA) method it is known [18] that the number of steps  $n$  that one needs to take in order to reach accuracy of order  $\varepsilon$  in the 2-Wasserstein distance is proportional to the condition number  $\kappa$  of the target covariance matrix  $\Sigma$ . For SK-ROCK, if one chooses<sup>4</sup> the number of stages  $s$  according to

$$s = \left\lceil \sqrt{\frac{\eta}{2}(\kappa - 1)} \right\rceil, \quad (3.5)$$

then the number of steps  $n$  for reaching accuracy of order  $\varepsilon$  now scales proportionally to  $\sqrt{\kappa}$ . This is illustrated in Figure 3, where we plot the number of steps  $n$  for a given accuracy  $\varepsilon$  as a function of the condition number  $\kappa$  for a two dimensional Gaussian target for EM and SK-ROCK. To make the comparison fair, for each of the methods we have chosen via a grid search the value of  $\delta$  that gives the lowest 2-Wasserstein distance for a given  $n, \kappa$ , and by setting  $s$  according to (3.5) with  $\eta = 0.05$ . As we can see in Figure 3, SK-ROCK requires significantly less gradient evaluations than the EM method used in MYULA, particularly for large condition numbers  $\kappa$ . This behaviour, and the corresponding behaviour of the number of steps  $n$  as a function of condition number  $\kappa$ , are indeed similar in nature to the behaviour of accelerated algorithms in optimisation [13].

### 3.3 Mean-square stability analysis

We conclude this section by presenting a mean-square stability analysis of SK-ROCK that explains its observed superiority over the EM method. In particular, we consider the following test equation that is widely used in the numerical analysis literature [28, 29] to benchmark SDE solvers

$$dX(t) = \gamma X(t)dt + \mu X(t)dW(t), \quad X(0) = 1, \quad (3.6)$$

<sup>3</sup>The proof is reported in Appendix A.

<sup>4</sup>the detailed rationale behind this choice can be found in the Appendix B

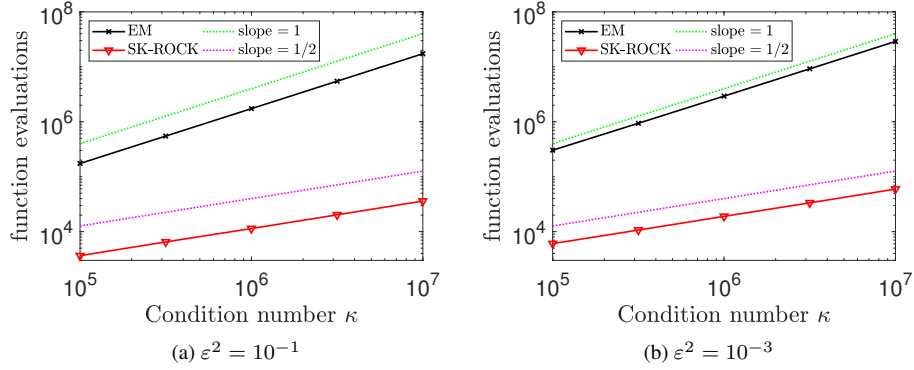


Figure 3: Wasserstein distance bounds, Gaussian analysis: Minimum number of function evaluations of the EM and SK-ROCK methods in order to have  $W_2(P; Q_n)^2 < \varepsilon^2$ , given different condition numbers  $\kappa$ .

where  $\gamma, \mu \in \mathbb{R}$ , which has the solution  $X(t) = \exp[(\gamma - 1/2\mu^2)t + \mu W(t)]$ . It is easy to show using Ito calculus that when  $2\gamma + |\mu|^2 < 0$

$$\lim_{t \rightarrow \infty} \mathbb{E}(|X(t)|^2) = 0.$$

We want to understand for what range of the time-steps  $\delta$  would a numerical discretisation  $X_n$  of (3.6) behave in a similar manner as  $n \rightarrow \infty$ , *i.e.*  $\mathbb{E}(|X_n|^2) \rightarrow 0$ . In the case of EM one has that

$$X_{n+1} = X_n + \delta\gamma X_n + \sqrt{\delta}\mu X_n Z_{n+1},$$

and hence

$$\mathbb{E}(|X_{n+1}|^2) = R(p, q)\mathbb{E}(|X_n|^2), \quad R(p, q) = (1 + p)^2 + q^2, \quad p = \delta\gamma, q = \sqrt{\delta}\mu.$$

We thus see that in order for  $\mathbb{E}(|X_n|^2) \rightarrow 0$  one needs that  $R(p, q) < 1$ . We visualise the values of admissible  $p, q$  for the EM method in Figure 4(b), where we can see that there is only a very small portion of the true mean square stability domain covered by it (anything on the left hand side of the dotted line in Figure 4(a)-(b) belongs to the true stability domain). That implies that when one or both of the parameters  $\gamma, \mu$  are large one needs to choose a very small  $\delta$  in order to be stable (for example when  $\mu = 0$  one recovers the stability condition  $\delta < -2\gamma^{-1}$  for the Langevin SDE). In the case of SK-ROCK one has that

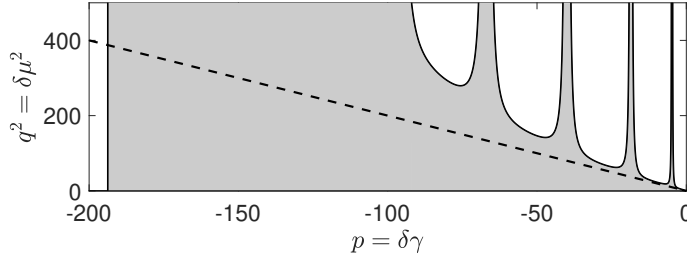
$$R(p, q) = R_1(p)^2 + R_2(p)^2 q^2$$

where  $R_1$  and  $R_2$  are given by (3.3).

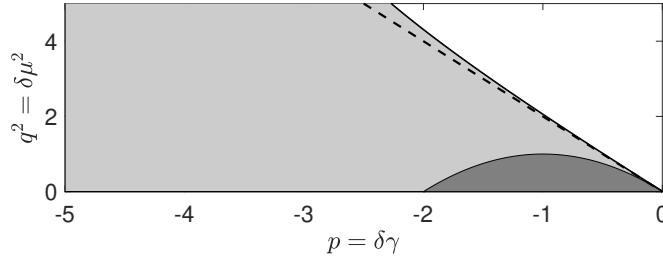
We now similarly to the case of the EM method plot the mean square stability domain of SK-ROCK in Figure 4(a). As we can see, a significantly larger portion of the true mean square stability domain is now covered when compared to the EM method. In fact, due to the properties of the Chebyshev polynomials the coverage of the stability domain is now quadratic in the number of stages  $s$  used in the algorithm, in contrast to  $s$ -steps of EM algorithm for which the coverage of the true stability domain would be linear in  $s$ . This means that for the same number of stages  $s$ , one can choose a much larger time-step  $\delta$  for SK-ROCK and still integrate equation (3.6) in a stable manner.

## 4 Numerical experiments

In this section we demonstrate the proposed SK-ROCK proximal MCMC methodology with a range of numerical experiments related to image deconvolution, tomographic reconstruction, and hyper-spectral unmixing. We have selected these experiments to represent a wide variety of configurations in terms of ill-posedness and ill-conditioning, strict and strong log-concavity, and dimensionality of  $y$  and  $x$ . We report comparisons with the MYULA method [20]



(a) SK-ROCK mean-square stability region ( $s = 10, \eta = 0.05$ )



(b) zoomed version of Figure 4(a) with EM mean-square stability region in dark grey

Figure 4: Mean-square stability domains for (a) SK-ROCK (with  $s = 10$ ) and (b) its zoomed version with the EM mean-square stability domain in dark grey ( $p - q^2$  plane). The dashed line represents the upper boundary of the true mean-square stability domain.

to highlight the benefits of using the SK-ROCK discretization as opposed to the conventional EM discretization used in Langevin and Hamiltonian algorithms [44], and because MYULA underpins other proximal MCMC algorithms such as the auxiliary Gibbs sampler of [53]. To make the comparisons fair, in all experiments we use the same number of gradient and proximal operator evaluations for MYULA and SK-ROCK, and compare their computational efficiency in terms of the effective sample size (ESS) of the generated chains<sup>5</sup> as this determines the accuracy of the Monte Carlo approximation. Notice that because the methods are compared at equal computational budget they do not produce the same number of samples, as their complexity per iteration is different. More precisely, if the MYULA chain has  $n$ -samples, then the SK-ROCK chain has only  $n/s$  samples, which is considerably lower. However, experiments show that SK-ROCK delivers significantly higher ESS values because of its superior convergence properties.

The samples obtained with MYULA and SK-ROCK can be used to compute a wide variety of Bayesian inferences. Because our aim is to demonstrate that SK-ROCK is computationally more efficient than MYULA, and our focus is on imaging problems, here we use the samples to compute two quantities: 1) the minimum mean square error solutions to the different considered problems, given by the posterior means; and 2) marginal posterior variances or standard deviations, that are more difficult to compute because they are second order moments and hence highlight the superior performance of SK-ROCK, and which provide an indication of the performance of the methods in uncertainty quantification tasks.

Moreover, we also use autocorrelation plots to visually compare the convergence properties of both methods. We compute the autorrelation functions for the fastest and the slowest components of the Markov chains, which represent the one-dimensional subspaces where the Markov chains achieve their highest and lowest convergence rates respectively, and that we determine via an estimate of the posterior covariance obtained from the chains. Again, to make the comparisons fair with regards to computational complexity, in all autocorrelation plots we apply a 1-in- $s$  thinning to the MYULA chain to artificially boost its autocorrelation function decay rate by a factor of  $s$ .

<sup>5</sup>Recall that  $ESS = n\{1 + 2\sum_k \rho(k)\}^{-1}$ , where  $n$  is the total number of samples and  $\sum_k \rho(k)$  is the sum of the  $K$  monotone sample auto-correlations which we estimated with the initial monotone sequence estimator [25].

Table 1: Values of the stepsize  $\delta$ , effective sample sizes (EES) and KL-divergence of the EM and SK-ROCK algorithms for the one dimensional Laplace distribution.

Stages $s$	Method	Stepsize $\delta$	ESS	KL-Divergence	Speed-up
-	MYULA	$1.0 \times 10^{-5}$	$3.6 \times 10^1$	$4.8 \times 10^{-2}$	-
$s = 10$	SK-ROCK	$1.7 \times 10^{-3}$	$6.0 \times 10^2$	$1.4 \times 10^{-2}$	16.67
$s = 15$	SK-ROCK	$4.0 \times 10^{-3}$	$9.5 \times 10^2$	$1.0 \times 10^{-2}$	26.39

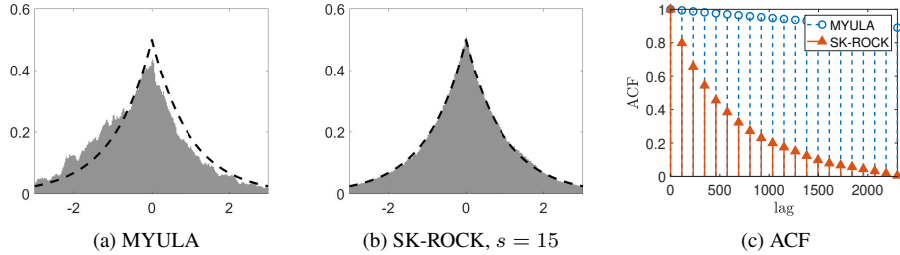


Figure 5: One-dimensional Laplace distribution: Histograms computed with (a)  $15 \times 10^6$  samples generated by MYULA and (b)  $15 \times 10^6/s$  samples generated by SK-ROCK from the approximated Laplace distribution, using an approximation parameter  $\lambda = 10^{-5}$  and  $s = 15$  for the SK-ROCK method. (c) Autocorrelation functions of the samples.

#### 4.1 One dimensional distributions

We start our numerical experiments by studying two simple one dimensional distributions, namely the Laplace distribution and the uniform distribution in  $[-1, 1]$ , for which we can also perform computations exactly. Since both of these distributions are not Lipschitz differentiable we employ the corresponding Moreau-Yosida approximation using  $\lambda = 10^{-5}$  to bring  $\pi_\lambda$  very close to  $\pi$  and deliver a good approximation. This implies that the largest stepsize  $\delta$  that can be used for MYULA is  $2 \times 10^{-5}$ , which is dramatically small. We set  $\delta = 10^{-5}$  for MYULA and run the corresponding chain for  $n = 15 \times 10^6$  iterations to create a situation where MYULA struggles to deliver a good approximation and that highlights the superior performance of SK-ROCK. For SK-ROCK we use  $s = 15$  and set  $\delta$  by using (add reference to rule here). Lastly, notice that we choose the (regularised) Laplace and the uniform distributions to illustrate the performance of the methods in two distinctly different scenarios: the regularised Laplace distribution is strongly log-concave near the mode and only strictly log-concave in the tails, which is problematic for the Langevin diffusion because the gradient remains constant as  $|x|$  grows, whereas the regularised uniform distribution is flat over  $[-1, 1]$  and hence has most of its mass in regions where the gradient is zero, and then strongly log-concave in the tails.

Figures 5 and 6 display the histogram approximations of the distributions obtained with the two methods, as well as the autocorrelation functions of the generated Markov chains. Observe that in both cases SK-ROCK significantly outperforms MYULA, which struggles to deliver a good approximation due to the stepsize limitation and the limited number of iterations (this phenomenon is particularly clearly captured by the difference in decay speed in the autocorrelation plots). These results are quantitatively summarised in Tables 1 and 2 respectively, where we highlight that SK-ROCK delivers an ESS that is over 25 times larger than MYULA, while also achieving higher accuracy as measured by the Kullback-Leibler (KL) divergence between the empirical distribution and  $\pi_\lambda$ . For completeness, we also report the results using SK-ROCK with  $s = 10$ .

It is worth emphasising at this point that we could improve the ESS performance of both methods by increasing the value of  $\lambda$ , at the expense of some additional bias. In the case of the uniform distribution this would lead to a considerable number of samples outside the true support  $[-1, 1]$ . See [20] for details.

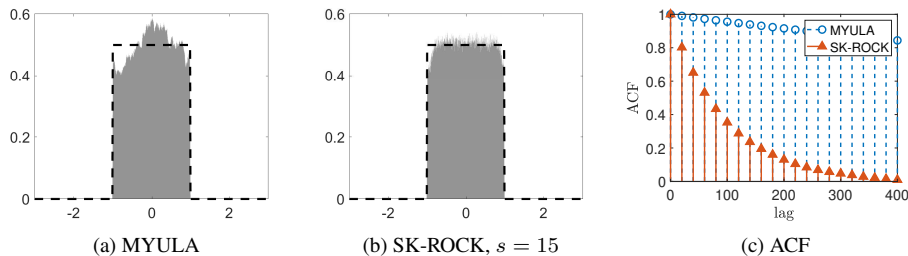


Figure 6: One-dimensional uniform distribution: Histograms computed with (a)  $15 \times 10^6$  samples generated by MYULA and (b)  $15 \times 10^6/s$  samples generated by SK-ROCK from the approximated uniform distribution, using an approximation parameter  $\lambda = 10^{-5}$  and  $s = 15$  for the SK-ROCK method. (c) Autocorrelation functions of the samples.

Table 2: Values of the stepsize  $\delta$ , effective sample sizes (EES) and KL-divergence of the EM and SK-ROCK algorithms for the one dimensional uniform distribution.

Stages $s$	Method	Stepsize $\delta$	ESS	KL-Divergence	Speed-up
-	MYULA	$1.0 \times 10^{-5}$	$1.7 \times 10^2$	$1.3 \times 10^{-2}$	-
$s = 10$	SK-ROCK	$1.7 \times 10^{-3}$	$3.4 \times 10^3$	$3.2 \times 10^{-2}$	20
$s = 15$	SK-ROCK	$4.0 \times 10^{-3}$	$4.9 \times 10^3$	$3.9 \times 10^{-2}$	28.82

## 4.2 Image deconvolution with total-variation prior

We now consider a non-blind image deconvolution problem, where we seek to recover a high-resolution image  $x \in \mathbb{R}^d$  from a blurred and noisy observation  $y = Hx + \epsilon$ , where  $H$  is a known blur operator and  $\epsilon \sim \mathcal{N}(0, \sigma^2 \mathbb{I}_d)$ . This problem is ill-conditioned i.e.,  $H$  is nearly singular, thus yielding highly noise-sensitive solutions. To make the estimation problem well posed, we use a total-variation norm prior that promotes solutions with spatial regularity. The resulting posterior distribution is given by

$$p(x|y) \propto \exp\left(-\|y - Hx\|^2/2\sigma^2 - \beta TV(x)\right), \quad (4.1)$$

where  $TV(x)$  represents the total-variation pseudo-norm [49, 15], and  $\sigma, \beta \in \mathbb{R}^+$  are model hyper-parameters that we assume fixed (in our experiments we use  $\beta = 0.047$ , determined using the method of [24]).

Figure 7 presents an experiment with the `cameraman` test image of size  $d = 256 \times 256$  pixels, depicted in Figure 7(a). Figure 7(b) shows an artificially blurred and noisy observation  $y$ , generated by using a  $5 \times 5$  uniform blur and  $\sigma = 0.47$ , related to a blurred signal-to-noise ratio of 40dB. We use MYULA and SK-ROCK to draw Monte Carlo samples from (4.1) using  $\lambda = 10^{-3}$ . To make the comparison fair, we generate  $10^5$  samples using MYULA and  $10^5/s$  samples using SK-ROCK for  $s = 15$ . We then use the generated samples to compute two quantities: 1) the minimum mean squared error (MMSE) estimator of  $x|y$ , given by the posterior mean; and 2) the pixel-wise (marginal) posterior standard deviation, which provides an indication of the level of confidence in each pixel value, as measured by the model. This quantity is useful for highlighting features in the image that are difficult to accurately determine; in the case of in image deconvolution problems these are the exact locations of edges and contours in the image. Notice that computing standard deviations requires computing second order statistical moments, which is more difficult than estimating the posterior mean, and hence requires a larger number of effective samples to produce stable estimates.

Observe in Figures 7(c)-(f) that while the estimates of the posterior mean obtained with MYULA and SK-ROCK are visually similar, the estimates of the pixel-wise standard deviations obtained with SK-ROCK are noticeably more accurate and in agreement with the results obtained by sampling the true posterior with an asymptotically unbiased Metropolis algorithm (see [39, Example 4.1]). In particular, the standard deviations estimated with SK-ROCK accurately capture the uncertainty in the location of the contours in the image, whereas MYULA produces very noisy

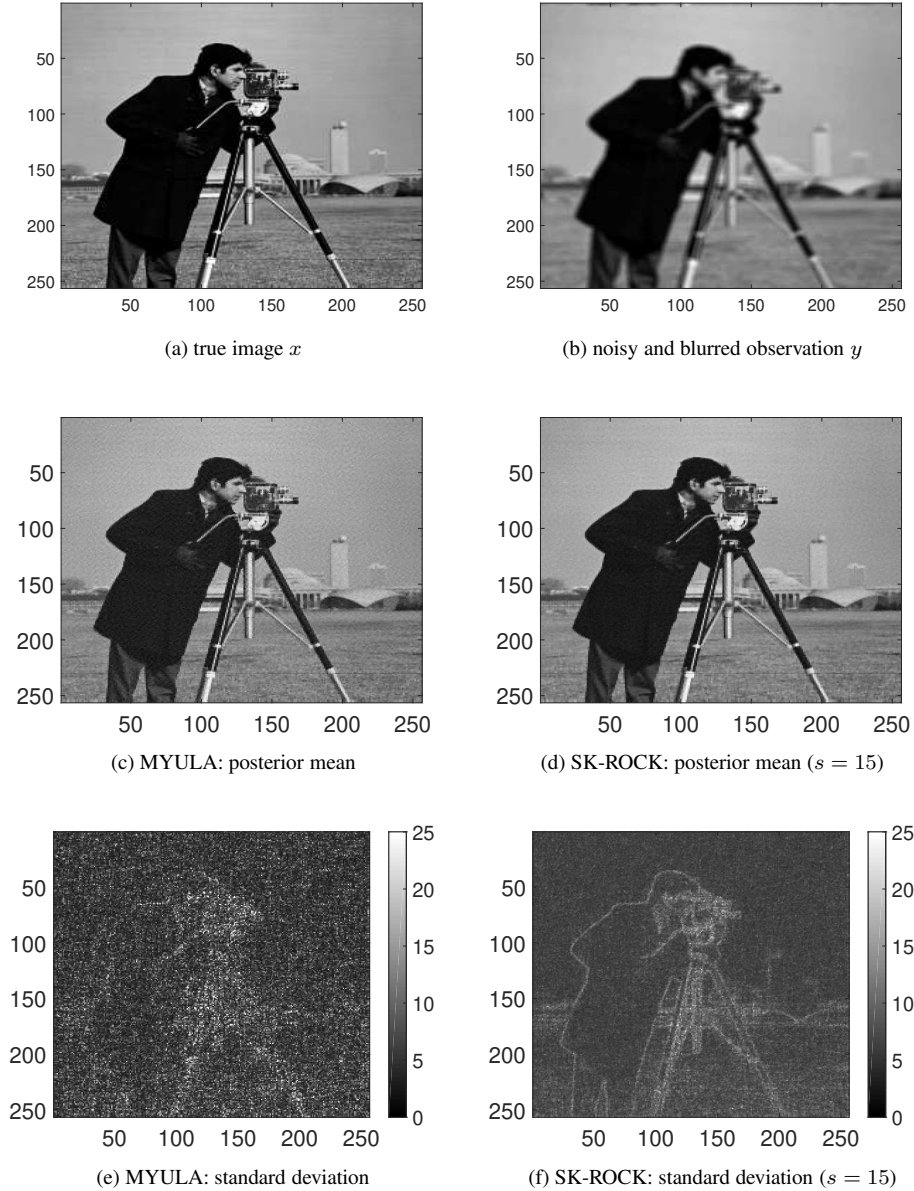


Figure 7: Cameraman experiment: (a) Original image of dimension  $256 \times 256$  pixels; (b) blurred observation with  $\text{SNR} = 40$ . (c) Mean of  $10^5$  samples generated by MYULA and (d) mean of  $10^5/s$  samples generated by SK-ROCK. (e) Standard deviation of the samples generated by MYULA and (f) SK-ROCK.

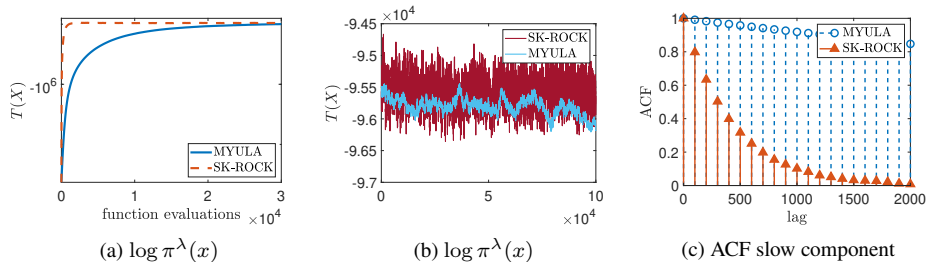


Figure 8: Cameraman experiment: (a) Convergence to the typical set of the posterior distribution (4.1) for the first  $3 \times 10^4$  MYULA samples and the first  $3 \times 10^4/s$  SK-ROCK ( $s = 15$ ) samples. (b) Last  $10^5$  values of  $\log \pi(x)$ . (c) Autocorrelation function for the slowest component.

Table 3: Cameraman experiment: Summary of the results after generating  $10^7$  samples with MYULA and  $10^7/s$  samples with SK-ROCK with  $s = 15$ . Computing time 35 hours per method.

Method	Stepsize $\delta$	ESS slow comp.	ESS fast comp.	Speed-up slow comp.	Speed-up fast comp.
MYULA	$9.9 \times 10^{-4}$	$3.5 \times 10^1$	$2.05 \times 10^4$	-	-
SK-ROCK ( $s = 10$ )	$1.7 \times 10^{-1}$	$3.3 \times 10^2$	$2.11 \times 10^5$	9.43	10.29
SK-ROCK ( $s = 15$ )	$4.0 \times 10^{-1}$	$6.4 \times 10^2$	$1.41 \times 10^5$	18.29	6.88

results as it struggles to estimate second order moments because of the stepsize limitation and limited computation budget (with a sufficiently large number of iterations, MYULA would produce similar results to SK-ROCK).

Moreover, to rigorously analyse the convergence properties of the two methods and compute autocorrelation functions, we generated  $10^7$  samples with MYULA and  $10^7/s$  samples using SK-ROCK ( $s = 15$ ). We then used these samples to determine the fastest and slowest components of each chain and measured their autocorrelation functions. We also computed trace plots for the chains by using  $T(x) = \log \pi_\lambda(x|y)$  as scalar statistic, which is particularly interesting because it determines the typical set of  $x|y$  [40]. These trace plots clearly illustrate how the methods behave during their transient regime, and then how they behave once the chains have converged to the typical set.

Figure 8(a) shows the convergence of the Markov chains to the typical set  $\{x : T(x) \approx \mathbb{E}[T(x)|y]\}$ . Observe that SK-ROCK converges significantly faster than MYULA, as expected given the acceleration properties of the method. Moreover, Figure 8(b) shows the last  $10^5$  samples of the chains (again with a 1-in- $s$  thinning for MYULA). Again, notice that SK-ROCK has significantly better mixing properties that result in a better exploration of the typical set. Lastly, the superior convergence properties of SK-ROCK are also clearly illustrated by the autocorrelation plots of Figure 8(c), which shows the autocorrelation functions for the slowest components of the chains, and where again we observe a dramatic improvement in decay rate (we have again used a 1-in- $s$  thinning for MYULA for fair comparison). Table 3 reports the associated ESS values for this experiment, where we note that SK-ROCK with  $s = 15$  outperforms MYULA by a factor of 18 in terms of computational efficiency for the slowest component. The autocorrelation functions for the fastest components of the chains exhibit a similar behaviour (see Table 3).

We conclude this experiment by comparing the two methods in terms of estimation of the MSE against the true image. Figure 9 shows the evolution of the estimation error for the MMSE solution, as estimated by MYULA and SK-ROCK, and as a function of the number of gradient and proximal operator evaluations. Again, observe that the acceleration properties of SK-ROCK lead to dramatic improvement in convergence speed, and consequently to a significantly more accurate computation of the MMSE estimator for given computational budget.

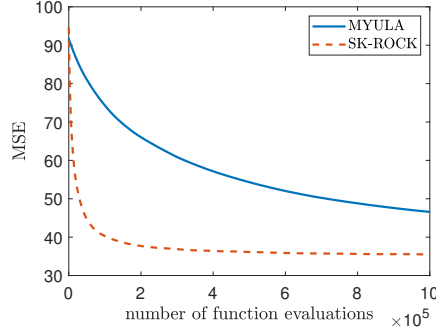


Figure 9: Cameraman experiment: Mean squared error (MSE) between the mean of the algorithms and the true image, measured using  $10^6$  samples from MYULA and  $10^6/s$  samples from SK-ROCK ( $s = 15$ ), in stationary regime.

### 4.3 Hyperspectral Unmixing

We now present an application to hyperspectral unmixing [33]. Given a hyperspectral image  $y \in \mathbb{R}^{m \times d}$  with  $m$  spectral bands and  $d$  pixels, the unmixing problem assumes that the observed scene is composed of  $k$  materials or *endmembers*, each with a characteristic spectral response  $a_j \in \mathbb{R}^m$  for  $j \in \{1, \dots, k\}$ , and seeks to determine the proportions or abundances  $x_{j,i}$  of each material  $j \in \{1, \dots, k\}$  in each image pixel  $i \in \{1, \dots, d\}$ . Here we consider the widely used linear mixing model  $y = Ax + w$ , where  $A = \{a_1, \dots, a_k\} \in \mathbb{R}^{m \times d}$  is a spectral library gathering the spectral responses of the materials,  $x \in \mathbb{R}^{k \times d}$  gathers the abundance maps, and  $w \sim \mathcal{N}(0, \sigma^2 \mathbb{I}_{m \times d})$  is additive Gaussian noise. Moreover, following [31], we expect  $x$  to be sparse since most image pixels contain only a subset of the materials. Also, we expect materials to exhibit some degree of spatial coherence and regularity. In order to promote solutions with these characteristics, we use the  $\ell_1$ -TV prior proposed in [31] for this type of problem

$$p(x) \propto \exp\{-\alpha \|x\|_1 - \beta TV(x)\} \mathbf{1}_{\mathbb{R}_+^n}(x)$$

where  $\alpha > 0$  and  $\beta > 0$  are hyper-parameters that we assume fixed (in our experiments we use  $\alpha = 25$  and  $\beta = 185$ , determined using the method of [24]). The resulting posterior distribution is given by [31]

$$p(x|y) \propto \exp[-\|y - Ax\|^2 / 2\sigma^2 - \alpha \|x\|_1 - \beta TV(x)] \mathbf{1}_{\mathbb{R}_+^n}(x). \quad (4.2)$$

Figure 10 presents an experiment with a synthetic dataset from [31] of size  $n = 75 \times 75 = 5625$ , with 5 materials, and noise amplitude  $\sigma = 8.4 \times 10^{-4}$  related to a signal-to-noise-ratio of 40dB (see [31] for details). Figure 10(a) presents the evolution of the estimation MSE between the true abundance maps and the posterior mean as estimated by MYULA and SK-ROCK (with  $s = 15$ ), and as a function of the number of gradient and proximal operator evaluations (using  $\lambda = 7.08 \times 10^{-7}$ ). As in previous experiments, observe that the posterior means estimated with SK-ROCK converge dramatically faster than the ones calculated with MYULA, clearly exhibiting the benefits of the proposed methodology. Moreover, for illustration, Figures 10(c)-(e) respectively show the estimated abundance maps for the fourth endmember for MYULA ( $5 \times 10^5$  samples) and SK-ROCK ( $5 \times 10^5/s$  samples,  $s = 15$ ), as well as the pixel-wise (marginal) standard deviations for the abundances of this material. Again, as in previous experiments, we notice that the estimates obtained with SK-ROCK are noticeably more precise than the ones of MYULA, which would require a larger number of iterations to accurately estimate these second order statistical moments.

To further compare the convergence properties of the two methods we repeated the experiment and generated  $5 \times 10^6$  samples with MYULA and  $5 \times 10^6/s$  samples with SK-ROCK for  $s = 15$  to make the comparisons fair. Figure 11(a) presents trace plots for the two chains during their transient regimes using  $T(x) = \log p(x|y)$  as summary statistic, as a function of the number of gradient and proximal operator evaluations; observe that SK-ROCK attains the typical set of  $x|y$  significantly faster than MYULA, similarly to the previous experiments. Figure 11(b) presents similar trace plots for the two chains in stationarity; again, observe that the SK-ROCK chain exhibits better mixing properties. The good convergence properties of SK-ROCK can be clearly observed in the autocorrelation plots of

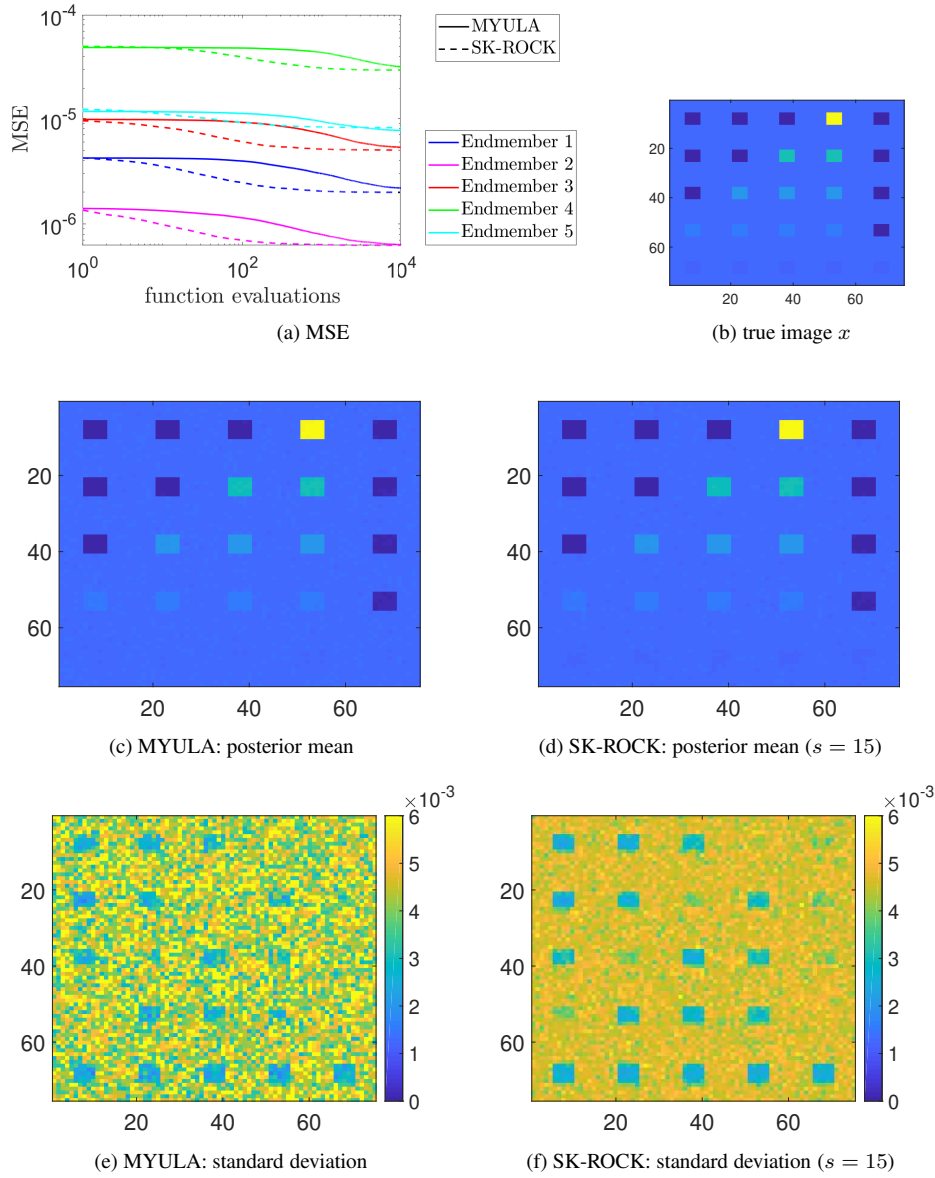


Figure 10: Hyperspectral experiment: (a) Mean squared error (MSE) between the mean of the algorithms and the true image (fractional abundances of endmembers 1 to 5) measured using  $10^4$  samples from MYULA (solid line) and  $10^4/s$  samples from SK-ROCK (dash-dot line,  $s = 15$ ), in logarithmic scale. (b) True fractional abundances of the endmember 4 ( $75 \times 75$  pixels), (c) posterior mean as estimated with  $10^5$  samples generated with MYULA and (d)  $10^5/s$  samples generated by SK-ROCK. (e) Standard deviation of the samples generated by MYULA and (f) SK-ROCK.

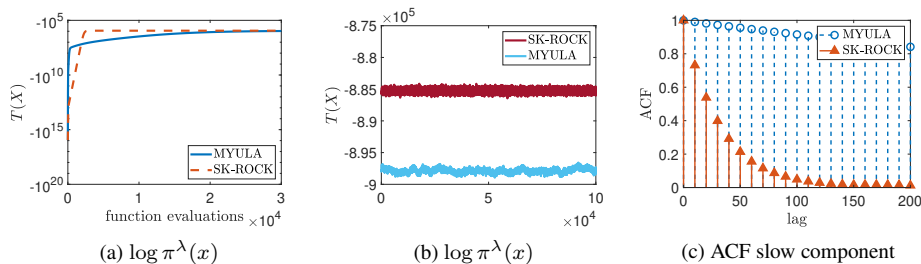


Figure 11: Hyperspectral experiment: (a) Convergence to the typical set of the posterior distribution (4.2) for the first  $3 \times 10^4$  MYULA samples and the first  $3 \times 10^4/s$  SK-ROCK ( $s = 15$ ) samples. (b) Last  $10^5$  values of  $\log \pi(x)$ . (c) Autocorrelation function for the slowest component.

Table 4: Hyperspectral experiment: Summary of the results after generating  $5 \times 10^6$  samples with MYULA and  $5 \times 10^6/s$  samples with SK-ROCK. Computing time 88 hours per method.

Method	Stepsize $\delta$	ESS slow comp.	ESS fast comp.	Speed-up slow comp.	Speed-up fast comp.
MYULA	$1.79 \times 10^{-9}$	$1.50 \times 10^2$	$0.63 \times 10^4$	-	-
SK-ROCK ( $s = 10$ )	$3.11 \times 10^{-7}$	$2.90 \times 10^3$	$1.70 \times 10^4$	19.33	2.69
SK-ROCK ( $s = 15$ )	$7.28 \times 10^{-7}$	$5.69 \times 10^3$	$3.63 \times 10^4$	37.93	5.76

Figure 11(c), which correspond to the slowest components of the chains as determined by their covariance structure, and where we have again applied the 1-in-15 thinning to the MYULA chain for fairness of comparison. Table 4 reports the ESS values for this experiment. In particular, observe that SK-ROCK outperforms MYULA by a factor of 37.9 in terms of ESS for the slowest component of the chain, and by a factor of 5.76 for the fastest component.

#### 4.4 Tomographic image reconstruction

We conclude this section with a tomographic image reconstruction experiment. We have selected this problem to illustrate the proposed methodology in a setting where the posterior distribution is strictly log-concave. The lack of strong log-concavity has a clear negative impact on the convergence properties of the continuous-time Langevin SDE (2.3) [19], and also impacts the convergence properties of the MYULA and SK-ROCK approximations.

In tomographic image reconstruction we seek to recover an image  $x \in \mathbb{R}^d$  from an observation  $y \in \mathbb{C}^p$  related to  $x$  by a linear Fourier model  $y = AFx + \xi$ , where  $F$  is the discrete Fourier transform operator on  $\mathbb{C}^d$ ,  $A \in \mathbb{C}^{p \times d}$  is a (sparse) tomographic subsampling mask and  $\xi \sim N(0, \sigma^2 \mathbb{I}_{2p})$ . Typically  $d \gg p$ , making the estimation problem strongly ill-posed. We address this difficulty by using a total-variation prior to regularise the estimation problem and promote solutions with certain spatial regularity properties. From Bayes' theorem, the posterior  $p(x|y)$  is given by:

$$p(x|y) \propto \exp \left[ -\|y - AFx\|^2 / 2\sigma^2 - \beta TV(x) \right], \quad (4.3)$$

with hyper-parameters  $\sigma, \beta \in \mathbb{R}^+$  assumed fixed (in our experiments we use  $\beta = 10^3$ ).

Figure 12 presents an experiment with the Shepp-Logan phantom test image of size  $d = 128 \times 128$  pixels, which we use to generate a noisy observation  $y$  by measuring 15% of the original Fourier coefficients, corrupted with additive Gaussian noise with  $\sigma = 7 \times 10^{-4}$  (to improve visibility, Figure 12(b) shows the amplitude of the Fourier coefficients in logarithmic scale, unobserved coefficients are depicted in black). Following on from this, we use MYULA and SK-ROCK with  $s = 10$  to generate  $10^5$  and  $10^4$  samples respectively from  $p(x|y)$  with  $\lambda = 10^{-7}$ . We then use said samples to compute the MMSE estimators - displayed in Figures 13(c)-(d) - as well as the (marginal) standard deviations of the amplitude of the Fourier coefficients of  $x|y$  depicted in logarithmic scale in Figures 13(e)-(f). We observe that in this case both methods deliver good and similar results with the number of samples available, with

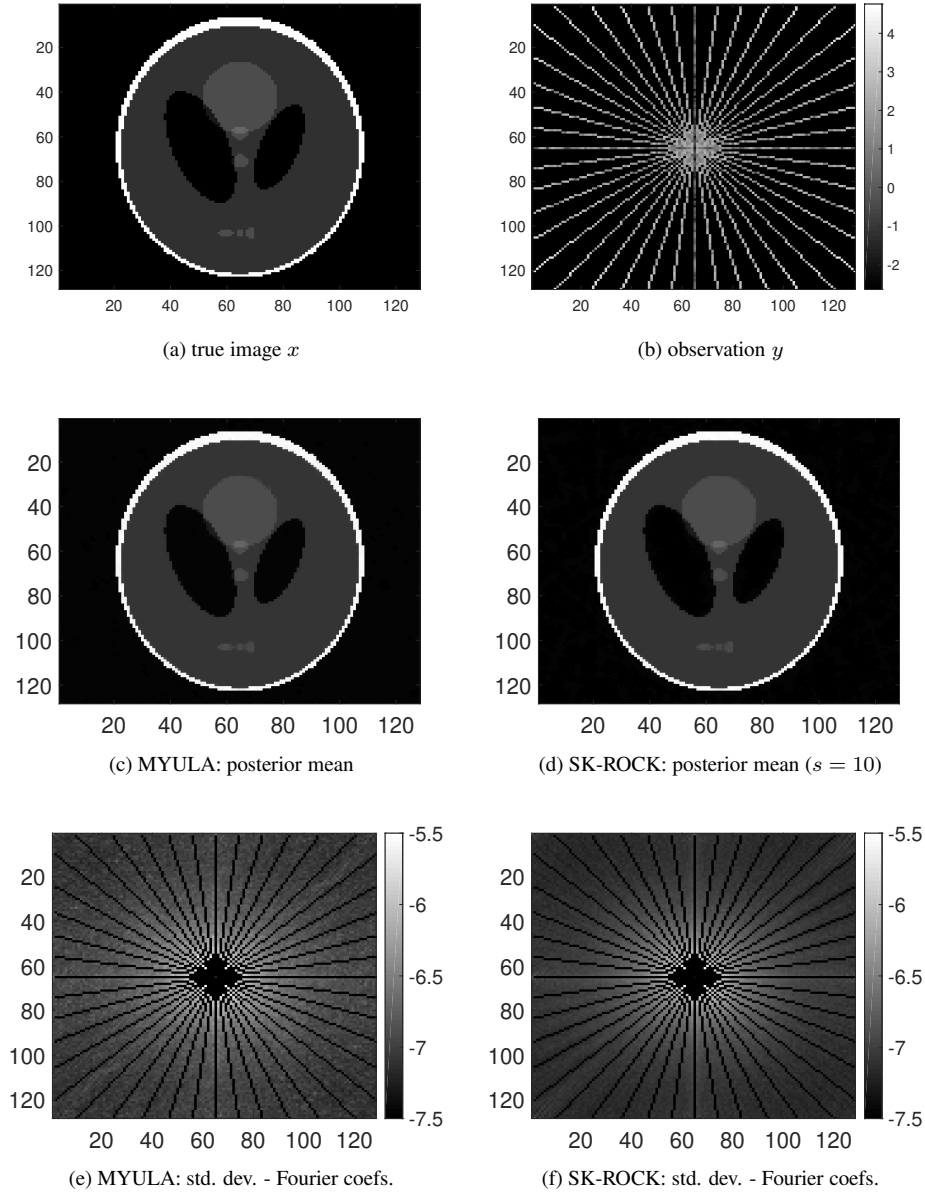


Figure 12: Tomography experiment: (a) Shepp–Logan phantom image ( $128 \times 128$  pixels), (b) tomographic observation  $y$  (amplitude of Fourier coefficients in logarithmic scale). Posterior mean of  $x|y$  as estimated with (c) MYULA ( $10^4$  samples) and (d) SK-ROCK ( $10^3$  samples,  $s = 10$ ). Standard deviations of the amplitude of the Fourier coefficients of  $x|y$  as estimated with (e) MYULA ( $10^4$  samples) and (f) SK-ROCK ( $10^3$  samples,  $s = 10$ ).

MYULA producing very mildly less accurate standard deviation estimates. More interestingly, notice from Figures 13(e)-(f) that in this tomographic experiment the uncertainty is concentrated in the unobserved medium frequencies, whereas in the deconvolution experiment uncertainty was predominant in the high-frequencies.

Moreover, to analyse the convergence properties of the two methods we compute autocorrelation functions by generating  $5 \times 10^6$  samples with MYULA and  $5 \times 10^6/s$  samples using SK-ROCK with  $s = 10$ . We use said samples to determine the fastest and slowest components of each chain and measure their autocorrelation functions. Table 5 reports the associated ESS, which show that the SK-ROCK outperform MYULA by a factor of 18.26 in terms of ESS for the slowest component of the chain, and by a factor of 3.33 for the fastest component. These superior convergence properties can be clearly observed in Figure 13(c), which presents the autocorrelation plots for the slowest components of the chains. For completeness, Table 5 also reports the values obtained with SK-ROCK with  $s = 5$ .

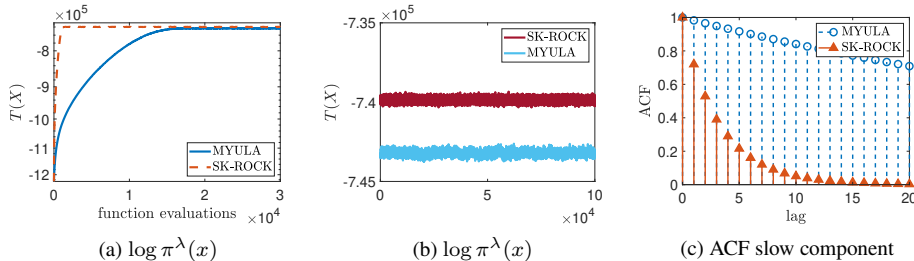


Figure 13: Tomography experiment: (a) Convergence to the typical set of the posterior distribution (4.3) for the first  $3 \times 10^4$  MYULA samples and the first  $3 \times 10^4/s$  SK-ROCK ( $s = 10$ ). (b) Last  $10^5$  values of  $\log \pi(x)$  from MYULA and SK-ROCK ( $s = 10$ ) chains. (c) Autocorrelation function for the slowest component.

Table 5: Tomography experiment: Summary of the results after generating  $5 \times 10^6$  samples with MYULA and  $5 \times 10^6/s$  samples with SK-ROCK. Computing time 20 hours per method.

Method	Stepsize $\delta$	ESS slow comp.	ESS fast comp.	Speed-up slow comp.	Speed-up fast comp.
MYULA	$8.33 \times 10^{-8}$	$4.14 \times 10^3$	$8.01 \times 10^4$	-	-
SK-ROCK ( $s = 5$ )	$2.51 \times 10^{-6}$	$3.09 \times 10^4$	$2.46 \times 10^5$	7.46	3.07
SK-ROCK ( $s = 10$ )	$1.15 \times 10^{-5}$	$7.56 \times 10^4$	$2.67 \times 10^5$	18.26	3.33

## 5 Discussion and conclusion

This paper presented a new proximal MCMC method that significantly outperforms existing proximal approaches for Bayesian computation in inverse problems related to imaging sciences. As in the case of previous proximal MCMC methods, the methodology is derived from a Moreau-Yoshida regularised overdamped Langevin diffusion process. However, the previous approaches relied on a simple Euler explicit discrete-time approximation of the Langevin process, and hence struggled to address ill-posed and ill-conditioned problems because of the corresponding severe time-step restrictions. The same type of computational issues arise in the case of gradient descent and proximal gradient optimisation algorithms, and have been successfully addressed by using accelerated proximal optimisation algorithms [8]. Our proposed methodology achieves a similar acceleration quality by using a sophisticated discretisation strategy that alleviates the time-step restrictions of explicit discretisations. For Gaussian models, we prove rigorously the acceleration of the Markov chains in the 2-Wasserstein distance as a function of the condition number  $\kappa$ . The superior behaviour of our method is further demonstrated with a range of numerical experiments, including non-blind image deconvolution, tomographic reconstruction, and hyperspectral unmixing, with total-variation and  $\ell_1$  priors. The generated Markov chains exhibit faster mixing, achieve larger effective sample sizes, and produce lower mean square

estimation errors at equal computational budget. This allows, for example, to accurately estimate high order statistical moments and perform uncertainty quantification analyses in a more computationally efficient way.

Furthermore, this paper opens a number of interesting directions for future research. For example, to theoretically analyse the non-asymptotic convergence properties of SK-ROCK for non-Gaussian log-concave models and derive bounds in total-variation and Wasserstein metrics; this is highly technical and will probably require developing new analysis techniques. Also, to investigate a Metropolis-adjusted variant of the stochastic Runge-Kutta-Chebyshev methods discussed in this paper. It would also be interesting to use SK-ROCK within the Gibbs splitting scheme of [53], and to investigate empirical Bayesian computation algorithms that combine SK-ROCK with stochastic gradient descent, which could be useful for estimating unknown model parameters such as regularisation parameters (e.g., see [24]).

## A Wasserstein distance - Gaussian process

We begin computing the distribution  $Q_n$  of the  $n$  samples generated by the approximation (3.2). We will work in the one dimensional case but the results easily extend to higher dimensions, as can be seen later. First, we can notice that the solution of (3.2) can be expressed by the following recursive formula:

$$X_n = (R_1(z))^n X_0 + \sqrt{2\delta} \sum_{i=1}^n (R_1(z))^{n-i} (R_2(z)) \xi_i,$$

where  $X_0$  is the initial condition of the problem. Computing expectations on both sides of the latter equation, we have:

$$\mathbb{E}(X_n) = (R_1(z))^n X_0.$$

Then, we compute the variance as follows:

$$\begin{aligned} \mathbb{E}(X_n^2) - \mathbb{E}(X_n)^2 &= 2\delta \sum_{i=1}^n (R_1(z))^{2(n-i)} (R_2(z))^2 \\ &= 2\delta (R_1(z))^{2n} (R_2(z))^2 \sum_{i=1}^n \frac{1}{(R_1(z))^{2i}} \\ &= 2\delta (R_1(z))^{2n} (R_2(z))^2 \frac{1}{(R_1(z))^2} \left[ \frac{1 - \frac{1}{(R_1(z))^{2n}}}{1 - \frac{1}{(R_1(z))^2}} \right] \\ &= 2\delta (R_2(z))^2 \left[ \frac{(R_1(z))^{2n} - 1}{(R_1(z))^2 - 1} \right], \end{aligned}$$

thus, the approximated distribution  $Q_n$  of the  $n$ -th sample produced by the numerical scheme (3.2) is defined, as follows:

$$Q_n = \mathcal{N} \left( (R_1(z))^n X_0, 2\delta (R_2(z))^2 \left[ \frac{(R_1(z))^{2n} - 1}{(R_1(z))^2 - 1} \right] \right).$$

We can now compute the Wasserstein distance between the two univariate Gaussian distributions  $P$  and  $Q_n$ :

$$W_2(P; Q_n)^2 = (R_1(z))^{2n} X_0^2 + \left[ \sigma - \sqrt{2\delta} R_2(z) \left( \frac{1 - (R_1(z))^{2n}}{1 - (R_1(z))^2} \right)^{1/2} \right]^2.$$

We can trivially extend the last result for a  $d$ -dimensional Gaussian distribution i.e. let  $P \sim N(0, \Sigma)$  where  $\Sigma = \text{diag}(\sigma_1^2, \dots, \sigma_d^2)$  and  $X_0 = (x_0^1, \dots, x_0^d)^T$  and obtain the following expression for the Wasserstein distance:

$$W_2(P; Q_n)^2 = \sum_{i=1}^d (R_1(z_i))^{2n} (x_0^i)^2 + \sum_{i=1}^d \left[ \sigma_i - \sqrt{2\delta} R_2(z_i) \left( \frac{1 - (R_1(z_i))^{2n}}{1 - (R_1(z_i))^2} \right)^{1/2} \right]^2,$$

where  $z_i = -\delta/\sigma_i^2$ . This concludes the proof.

## B Explicit bound for the Wasserstein distance

We begin applying the triangle inequality to  $W_2(P; Q_{n+1})^2$  as follows:

$$W_2(P; Q_{n+1})^2 \leq W_2(P; \tilde{Q})^2 + W_2(\tilde{Q}; Q_{n+1})^2, \quad (\text{B.1})$$

where  $\tilde{Q}$  is the unique invariant distribution to which (3.2) converges when  $n \rightarrow \infty$  and it is defined as:

$$\tilde{Q} = \mathcal{N} \left( 0, 2\delta(R_2(z))^2 \left[ \frac{1}{1 - (R_1(z))^2} \right] \right),$$

thus, we have that:

$$\begin{aligned} W_2(\tilde{Q}; Q_{n+1})^2 &= \sum_{i=1}^d R_1(z_i)^{2n+2} (x_0^i)^2 + \sum_{i=1}^d \left[ \left( \frac{2\delta R_2(z_i)^2}{1 - R_1(z_i)^2} \right)^{1/2} \right. \\ &\quad \left. - \sqrt{2\delta} R_2(z_i) \left( \frac{1 - R_1(z_i)^{2n+2}}{1 - R_1(z_i)^2} \right)^{1/2} \right]^2, \\ &= \sum_{i=1}^d \left[ R_1(z_i)^{2n+2} (x_0^i)^2 + \frac{2\delta R_2(z_i)^2}{1 - R_1(z_i)^2} \left( \sqrt{1} - \sqrt{1 - R_1(z_i)^{2n+2}} \right)^2 \right]. \end{aligned} \quad (\text{B.2})$$

It is easy to prove the following property:

$$\frac{1 - \sqrt{1 - x^{2n+2}}}{1 - \sqrt{1 - x^{2n}}} x^2 \leq x^2, \quad (\text{B.3})$$

for  $x \in (0, 1)$ . Thus, applying the latter in (B.2) we have:

$$\begin{aligned} W_2(\tilde{Q}; Q_{n+1})^2 &\leq \sum_{i=1}^d R_1(z_i)^{2n+2} (x_0^i)^2 + \sum_{i=1}^d \frac{2\delta R_2(z_i)^2}{1 - R_1(z_i)^2} \left( R_1(z_i)^2 \left[ 1 - \sqrt{1 - R_1(z_i)^{2n}} \right] \right)^2 \\ &\leq \sum_{i=1}^d \left[ R_1(z_i)^{2n} (x_0^i)^2 + \frac{2\delta R_2(z_i)^2}{1 - R_1(z_i)^2} \left( 1 - \sqrt{1 - R_1(z_i)^{2n}} \right)^2 \right] R_1(z_i)^2 \\ &\leq \max_{1 \leq i \leq d} R_1(z_i)^2 W_2(\tilde{Q}; Q_n)^2 \end{aligned}$$

Thus, (B.1) becomes:

$$W_2(P; Q_{n+1})^2 \leq W_2(P; \tilde{Q})^2 + \max_{1 \leq i \leq d} R_1(z_i)^2 W_2(\tilde{Q}; Q_n)^2.$$

Let:

$$C = \max_{1 \leq i \leq d} R_1(z_i)^2,$$

applying (B.3)  $n + 1$  times, we finally have that:

$$W_2(P; Q_{n+1})^2 \leq W_2(P; \tilde{Q})^2 + C^{n+1} W_2(\tilde{Q}; Q_0)^2,$$

concluding the proof.

As an attempt to minimise the bound found in the latter expression, we will try to accelerate the decay of the constant  $C$  composed by  $R_1(z)$  in the stochastic ROCK methods. This approach follows closely the approach in [21]. In particular, in order to bound  $R_1(z)$  by one, we need that  $|\omega_0 + \omega_1 z| \leq 1$ , in other words we need that:

$$-1 \leq \omega_0 - \omega_1 \frac{\delta}{\sigma_i^2} \leq 1.$$

Let  $L := 1/\sigma_{\min}^2$  and  $\ell := 1/\sigma_{\max}^2$ , so we have that:

$$-1 \leq \omega_0 - \omega_1 L \delta \leq \omega_0 - \omega_1 \ell \delta \leq 1,$$

which it is the same as:

$$-1 \leq \omega_1 \ell \delta - \omega_0 \leq \omega_1 L \delta - \omega_0 \leq 1.$$

Working with the first two members on the left-hand side of the latter inequality, we have that:

$$\delta \geq \frac{\omega_0 - 1}{\ell \omega_1}.$$

We choose the smallest  $\delta$  to have an efficient algorithm i.e.,  $\delta = (\omega_0 - 1)/\ell \omega_1$  and now working with the last two members on the right-hand side of the previous inequality, we have that:

$$\kappa := \frac{L}{\ell} \leq \frac{\omega_0 + 1}{\omega_0 - 1} = 1 + \frac{2s^2}{\eta}$$

where  $\kappa$  is the condition number of our Gaussian problem. We choose the smallest  $s$  to have an efficient algorithm and the latter expression determines the parameter  $s$  as:

$$s = \left\lceil \sqrt{\frac{\eta}{2}(\kappa - 1)} \right\rceil, \tag{B.4}$$

where  $\lceil x \rceil$  is the notation for the integer rounding of real numbers.

## References

- [1] A. ABDULLE, *Explicit stabilized Runge-Kutta methods*, Encyclopedia of Applied and Computational Mathematics, (2015), pp. 460–468.
- [2] A. ABDULLE, I. ALMUSLIMANI, AND G. VILMART, *Optimal explicit stabilized integrator of weak order one for stiff and ergodic stochastic differential equations*, SIAM/ASA Journal on Uncertainty Quantification, 6 (2018), pp. 937–964.
- [3] A. ABDULLE AND S. CIRILLI, *S-ROCK: Chebyshev methods for stiff stochastic differential equations*, SIAM Journal on Scientific Computing, 30 (2008), pp. 997–1014.
- [4] A. ABDULLE, G. VILMART, AND K. ZYGALAKIS, *High order numerical approximation of the invariant measure of ergodic sdes*, SIAM Journal on Numerical Analysis, 52 (2014), pp. 1600–1622.
- [5] M. V. AFONSO, J. M. BIOCAS-DIAS, AND M. A. T. FIGUEIREDO, *Fast image recovery using variable splitting and constrained optimization*, IEEE Transactions on Image Processing, 19 (2010), pp. 2345–2356.
- [6] S. ARRIDGE, P. MAASS, O. ÖKTEM, AND C.-B. SCHÖNLIEB, *Solving inverse problems using data-driven models*, Acta Numerica, 28 (2019), pp. 1–174.
- [7] Y. ATCHADE AND A. BHATTACHARYYA, *Regularization and Computation with high-dimensional spike-and-slab posterior distributions*, arXiv e-prints, (2018), p. arXiv:1803.10282.
- [8] A. BECK, *First-order methods in optimization*, vol. 25 of MOS-SIAM Series on Optimization, Society for Industrial and Applied Mathematics (SIAM), Philadelphia, PA; Mathematical Optimization Society, Philadelphia, PA, 2017.
- [9] A. BECK AND M. TEOULLE, *A fast iterative shrinkage-thresholding algorithm for linear inverse problems*, SIAM Journal on Imaging Sciences, 2 (2009), pp. 183–202.

- [10] P. BIANCHI, A. SALIM, AND S. SCHECHTMAN, *Passty langevin*, in Conference on Machine Learning (CML) 2019, Toulouse, France, June 2019.
- [11] N. BROSSE, A. DURMUS, M. PEREYRA, AND E. MOULINES, *Sampling from a log-concave distribution with compact support with proximal langevin monte carlo*, in Conference on Learning Theory (COLT) 2017, Amsterdam, Netherlands, Sep. 2017.
- [12] X. CAI, M. PEREYRA, AND J. D. MCEWEN, *Uncertainty quantification for radio interferometric imaging – I. Proximal MCMC methods*, Monthly Notices of the Royal Astronomical Society, 480 (2018), pp. 4154–4169.
- [13] Y. CARMON, J. C. DUCHI, O. HINDER, AND A. SIDFORD, *Accelerated methods for nonconvex optimization*, SIAM Journal on Optimization, 28 (2018), pp. 1751–1772.
- [14] L. CHAARI, J. TOURNERET, C. CHAUX, AND H. BATATIA, *A hamiltonian monte carlo method for non-smooth energy sampling*, IEEE Transactions on Signal Processing, 64 (2016), pp. 5585–5594.
- [15] A. CHAMBOLLE, *An algorithm for total variation minimization and applications*, Journal of Mathematical imaging and vision, 20 (2004), pp. 89–97.
- [16] A. CHAMBOLLE AND T. POCK, *An introduction to continuous optimization for imaging*, Acta Numerica, 25 (2016), pp. 161–319.
- [17] I. DAUBECHIES, M. DEFRISE, AND C. DE MOL, *An iterative thresholding algorithm for linear inverse problems with a sparsity constraint*, Communications on Pure and Applied Mathematics, 57 (2004), pp. 1413–1457.
- [18] A. DURMUS, S. MAJEWSKI, AND B. MIASOJEDOW, *Analysis of langevin monte carlo via convex optimization*, Journal of Machine Learning Research, 20 (2019), pp. 1–46.
- [19] A. DURMUS AND E. MOULINES, *Nonasymptotic convergence analysis for the unadjusted Langevin algorithm*, Annals of Applied Probability, 27 (2017), pp. 1551–1587.
- [20] A. DURMUS, E. MOULINES, AND M. PEREYRA, *Efficient Bayesian computation by proximal Markov chain Monte Carlo: when Langevin meets Moreau*, SIAM Journal on Imaging Sciences, 11 (2018), pp. 473–506.
- [21] A. EFTEKHARI, B. VANDEREYCKEN, G. VILMART, AND K. C. ZYGALAKIS, *Explicit stabilised gradient descent for faster strongly convex optimisation*, arXiv e-prints, (2018).
- [22] V. ELSER, T. LAN, AND T. BENDORY, *Benchmark problems for phase retrieval*, SIAM Journal on Imaging Sciences, 11 (2018), pp. 2429–2455.
- [23] C. ELVIRA, P. CHAINAIS, AND N. DOBIGEON, *Bayesian antisparsity coding*, IEEE Transactions on Signal Processing, 65 (2017), pp. 1660–1672.
- [24] A. FERNANDEZ VIDAL AND M. PEREYRA, *Maximum likelihood estimation of regularisation parameters*, in 2018 25th IEEE International Conference on Image Processing (ICIP), IEEE International Conference on Image Processing (ICIP), United States, 9 2018, IEEE, pp. 1742–1746.
- [25] C. J. GEYER, *Practical markov chain monte carlo*, Statistical Science, 7 (1992), pp. 473–483.
- [26] M. GIROLAMI AND B. CALDERHEAD, *Riemann manifold langevin and hamiltonian monte carlo methods*, Journal of the Royal Statistical Society: Series B (Statistical Methodology), 73 (2011), pp. 123–214.
- [27] P. J. GREEN, K. ŁATUSZYŃSKI, M. PEREYRA, AND C. P. ROBERT, *Bayesian computation: a summary of the current state, and samples backwards and forwards*, Statistics and Computing, 25 (2015), pp. 835–862.
- [28] D. J. HIGHAM, *A-stability and stochastic mean-square stability*, BIT Numerical Mathematics, 40 (2000), pp. 404–409.

- [29] D. J. HIGHAM, *Mean-square and asymptotic stability of the stochastic theta method*, SIAM Journal on Numerical Analysis, 38 (2000), pp. 753–769.
- [30] A. HOUDARD, C. BOUYEYRON, AND J. DELON, *High-dimensional mixture models for unsupervised image denoising (hdmi)*, SIAM Journal on Imaging Sciences, 11 (2018), pp. 2815–2846.
- [31] M.-D. IORDACHE, J. M. BIUCAS-DIAS, AND A. PLAZA, *Total variation spatial regularization for sparse hyperspectral unmixing*, IEEE Transactions on Geoscience and Remote Sensing, 50 (2012), pp. 4484–4502.
- [32] J. KAIPIO AND E. SOMERSALO, *Statistical and computational inverse problems*, vol. 160, Springer Science & Business Media, 2006.
- [33] N. KESHA AND J. MUSTARD, *Spectral unmixing*, IEEE Signal Processing Magazine, 19 (2002), pp. 44–57.
- [34] P. E. KLOEDEN AND E. PLATEN, *Numerical solution of stochastic differential equations*, vol. 23 of Applications of Mathematics (New York), Springer-Verlag, Berlin, 1992.
- [35] F. LUCKA, N. HUYNH, M. BETCKE, E. ZHANG, P. BEARD, B. COX, AND S. ARRIDGE, *Enhancing compressed sensing 4d photoacoustic tomography by simultaneous motion estimation*, SIAM Journal on Imaging Sciences, 11 (2018), pp. 2224–2253.
- [36] C. MARIE-CAROLINE, K. DENIS, C. EMILIE, T. JEAN-YVES, AND P. JEAN-CHRISTOPHE, *Preconditioned P-ULA for Joint Deconvolution-Segmentation of Ultrasound Images –Extended Version*, arXiv e-prints, (2019).
- [37] Y. MARNISSI, A. BENAZZA-BENYAHIA, E. CHOUZENOUX, AND J. . PESQUET, *Majorize-minimize adapted metropolis-hastings algorithm. application to multichannel image recovery*, in 2014 22nd European Signal Processing Conference (EUSIPCO), Sep. 2014, pp. 1332–1336.
- [38] Y. MARNISSI, E. CHOUZENOUX, J. PESQUEL, AND A. BENAZZA-BENYAHIA, *An auxiliary variable method for langevin based mcmc algorithms*, in 2016 IEEE Statistical Signal Processing Workshop (SSP), June 2016, pp. 1–5.
- [39] M. PEREYRA, *Proximal markov chain monte carlo algorithms*, Statistics and Computing, 26 (2016), pp. 745–760.
- [40] M. PEREYRA, *Maximum-a-posteriori estimation with bayesian confidence regions*, SIAM Journal on Imaging Sciences, 10 (2017), pp. 285–302.
- [41] M. PEREYRA, *Revisiting maximum-a-posteriori estimation in log-concave models*, SIAM Journal on Imaging Sciences, 12 (2019), pp. 650–670.
- [42] M. PEREYRA, J. M. BIUCAS-DIAS, AND M. A. T. FIGUEIREDO, *Maximum-a-posteriori estimation with unknown regularisation parameters*, in 2015 23rd European Signal Processing Conference (EUSIPCO), Aug 2015, pp. 230–234.
- [43] M. PEREYRA AND S. MCLAUGHLIN, *Comparing bayesian models in the absence of ground truth*, in 2016 24th European Signal Processing Conference (EUSIPCO), European Signal Processing Conference (EUSIPCO), United States, 12 2016, IEEE, pp. 528–532.
- [44] M. PEREYRA, P. SCHNITER, E. CHOUZENOUX, J.-C. PESQUET, J.-Y. TOURNERET, A. O. HERO, AND S. MCLAUGHLIN, *A survey of stochastic simulation and optimization methods in signal processing*, IEEE Journal of Selected Topics in Signal Processing, 10 (2016), pp. 224–241.
- [45] A. REPETTI, M. PEREYRA, AND Y. WIAUX, *Scalable bayesian uncertainty quantification in imaging inverse problems via convex optimization*, SIAM Journal on Imaging Sciences, 12 (2019), pp. 87–118.
- [46] C. ROBERT, *The Bayesian choice: from decision-theoretic foundations to computational implementation*, Springer Science & Business Media, 2007.

- [47] G. O. ROBERTS AND R. L. TWEEDIE, *Exponential convergence of langevin distributions and their discrete approximations*, Bernoulli, 2 (1996), pp. 341–363.
- [48] Y. ROMANO, M. ELAD, AND P. MILANFAR, *The little engine that could: Regularization by denoising (red)*, SIAM Journal on Imaging Sciences, 10 (2017), pp. 1804–184.
- [49] L. I. RUDIN, S. OSHER, AND E. FATEMI, *Nonlinear total variation based noise removal algorithms*, Physica D: nonlinear phenomena, 60 (1992), pp. 259–268.
- [50] B. P. SUTTON, D. C. NOLL, AND J. A. FESSLER, *Fast, iterative image reconstruction for mri in the presence of field inhomogeneities*, IEEE Transactions on Medical Imaging, 22 (2003), pp. 178–188.
- [51] M. VONO, N. DOBIGEON, AND P. CHAINAIS, *Sparse bayesian binary logistic regression using the split-and-augmented gibbs sampler*, in 2018 IEEE 28th International Workshop on Machine Learning for Signal Processing (MLSP), Sep. 2018, pp. 1–6.
- [52] M. VONO, N. DOBIGEON, AND P. CHAINAIS, *Bayesian image restoration under poisson noise and log-concave prior*, in ICASSP 2019 - 2019 IEEE International Conference on Acoustics, Speech and Signal Processing (ICASSP), May 2019, pp. 1712–1716.
- [53] M. VONO, N. DOBIGEON, AND P. CHAINAIS, *Split-and-augmented Gibbs sampler - Application to large-scale inference problems*, IEEE Transactions on Signal Processing, 67 (2019), pp. 1648–1661.
- [54] A. WIBISONO, A. C. WILSON, AND M. I. JORDAN, *A variational perspective on accelerated methods in optimization*, Proceedings of the National Academy of Sciences, 113 (2016), pp. E7351–E7358.
- [55] D. WIPF AND H. ZHANG, *Revisiting bayesian blind deconvolution*, Journal of Machine Learning Research, 15 (2014), pp. 3775–3814.
- [56] J. YE, Y. HAN, AND E. CHA, *Deep convolutional framelets: A general deep learning framework for inverse problems*, SIAM Journal on Imaging Sciences, 11 (2018), pp. 991–1048.